Dynamics of Atmospheres and Oceans 100 (2022) 101336

Contents lists available at ScienceDirect

Dynamics of Atmospheres and Oceans

journal homepage: www.elsevier.com/locate/dynatmoce

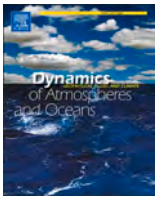

KmT, Kilometer-long mooring of high-resolution Temperature measurements results overview

Hans van Haren

NIOZ Royal Netherlands Institute for Sea Research, P.O. Box 59, 1790 AB Den Burg, the Netherlands

ARTICLE INFO

Keywords:
Kilometer long thermistor string
Mooring observations
Breaking internal waves
Mount Josephine
Turbulence above slope
Turbulence in interior

ABSTRACT

The global oceans show extensive bottom topography above which intensive turbulent mixing is generated by breaking internal waves. Growing evidence suggests that the mixing is sufficient to maintain the ocean's stable vertical density stratification, thereby preventing the deep-ocean from becoming a stagnant pool of cold water. Observational details of the extent of turbulent mixing away from topography are still scarce however. In this paper, results are presented from 760 high-resolution temperature sensors that were moored between 8 and 1146.5 m above a 2380-m deep sloping seafloor of Mount Josephine NE-Atlantic for 4 months. The local seafloor-slope is supercritical for semidiurnal internal tides under average stratification. The purpose of the $>$ 1-km-long densely instrumented mooring is to provide insight in the variability of coherent scales, and in the connection between seamount-slope and mixing-effects up to 7-km horizontally into the ocean-interior. Largest four-month mean turbulence values are found near the seafloor, decreasing to half an order of magnitude lower values at 500 m above, and remaining steady-high further up. Local increases of mean turbulence values are observed in bands of 100–200 m thickness. Larger internal wave breaking occurs during baroclinic spring tide, which also affects internal waves and turbulent overturning in the interior. Spectrally, a turbulence inertial sub-range dominates part of the internal wave band continuum near the seafloor. Coupling between interior- and near-seafloor-mixing is not only via previously suggested isopycnal transport of mixed waters, but also via strong internal wave interactions. Seamount-flow contributes to absolute vorticity so that blue-shifted near-inertial motions interact with internal tides.

1. Introduction

It is not unexpected that the ocean is turbulent everywhere considering its scales, but some places are more turbulent than others. The more turbulent places are important for ocean-life and for transport of suspended matter. Half a century ago, underwater topography has been recognized as one of the more turbulent places. Since Munk (1966)'s suggestion with follow-ups by Wunsch (1970) and Armi (1978) that most ocean-mixing occurs in the vicinity of sloping seafloor topography, efforts have been made to establish the dominant processes until to date. See for example a recent overview on the importance of internal waves generated by flow over topography (Sarkar and Scotti, 2017).

Wunsch (1972) demonstrated the influence of Bermuda Island on ocean turbulence using limited shipborne Conductivity-Temperature-Depth (CTD) profiling and moored current meter observations. In the ocean-interior, the water-flow is essentially geostrophic and the effect of turbulent mixing is to increase the geostrophic shear within one Rossby deformation radius

E-mail address: hans.van.haren@nioz.nl.

https://doi.org/10.1016/j.dynatmoce.2022.101336
Received 18 May 2022; Received in revised form 14 September 2022; Accepted 17 October 2022
Available online 19 October 2022

L_{ROi} from the island, possibly leading to further instabilities. $L_{ROi} = Nh/f \approx 2$ km for mid-ocean mid-latitude data, where h = 100 m denotes a vertical mixing scale, N the 100-m scale buoyancy frequency and f the local inertial frequency. The L_{ROi} indicates the horizontal extent of a patch of mixed water along isopycnals before rotation takes effect, and the extent of (in)coherent signals (Wunsch and Dahlen, 1970; Wunsch, 1972; Dale et al., 2006). In this picture of a turbulent mixing field, the near-shore temperature and velocity fluctuations are forced either by the mean flow, or by breaking internal waves that need not necessarily behave like freely propagating internal waves.

Armi (1978) presented profiles of salinity and potential temperature in the deep ocean and suggested the characteristic signature of two complementary mixing processes. Vertical mixing was considered to occur within 50-m-thick layers at boundaries and topographic features. Lateral advection and eventual smearing of these mixed layers was considered to occur horizontally along iopycnal surfaces. The combined effect of these two processes is often parametrically disguised as a vertical eddy diffusivity in one-dimensional models (Armi, 1979). While these suggestions are accurate at large, the details of the vertical and horizontal mixing away from sloping topography are under debate with renewed modeling efforts (e.g., Winters, 2015). Internal wave breaking seems to induce more mixing and at larger scales than frictional flow over underwater topography. The horizontal extent of isopycnal mixing seems $O(L_{Roi})$, which is rather smaller than O(100) km following water mass anomalies in layers traced between different profiles of observables obtained some distance apart (Armi, 1978; 1979; Schmitt, 1987). Possibly, a mix-up confuses between active turbulence and advective transport of mixed waters.

As frictional boundary layers are generally too small, extending up to 10 m above a flat seafloor and about 30 m above a sloping seafloor (Weatherly and Martin, 1978), or create a slippery boundary above sloping topography (MacCready and Rhines, 1991), the only candidate for sufficient deep-ocean turbulent mixing is the breaking of internal waves. Above steep sloping topography most internal wave breaking occurs, as suggested by Wunsch (1970; 1972) and, e.g., Armi (1978), Eriksen (1982), Thorpe (1987), Sarkar and Scotti (2017).

The assumption to maintain the entire ocean vertically stably stratified in density, without the need of further mixing in the

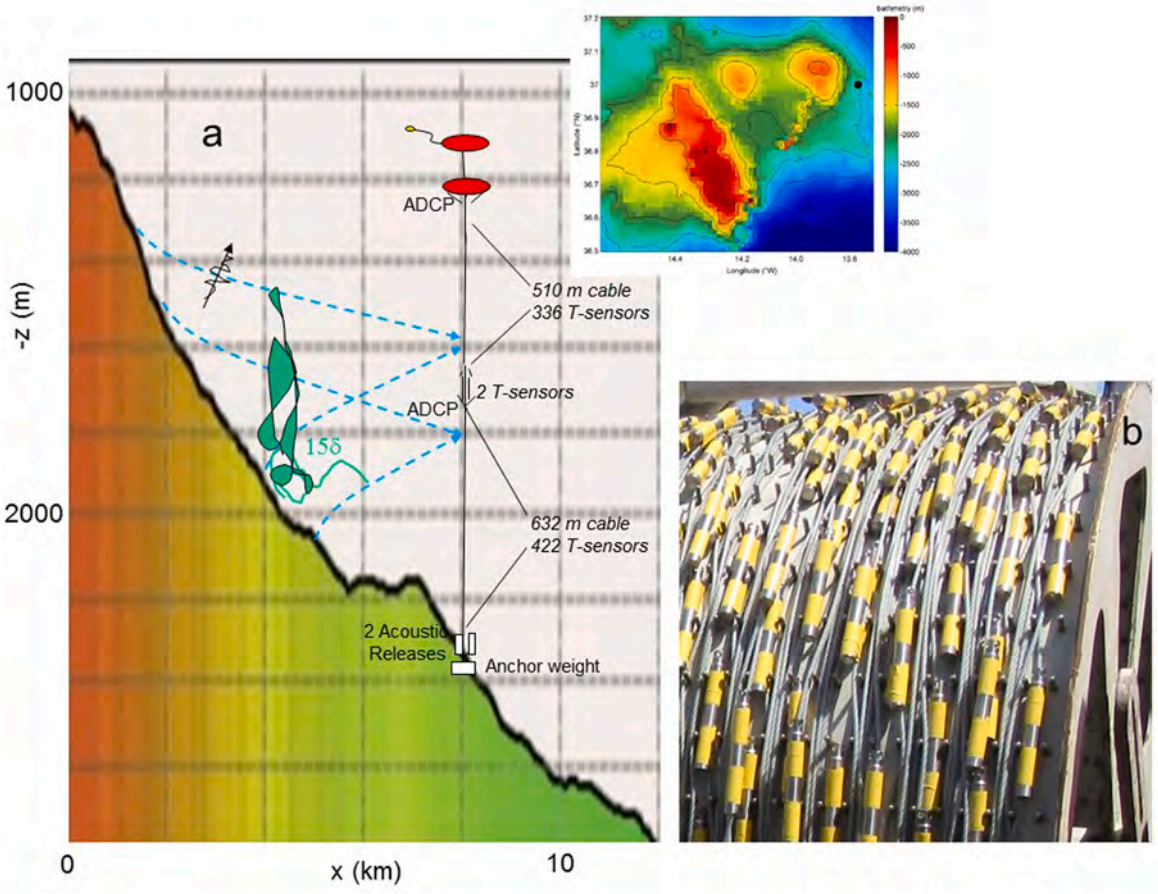

Fig. 1. Mooring information. (a) East-west Multibeam transect along 37°00N of the bathymetry of Mount Josephine around the mooring site, drawn in an aspect ratio of vertical:horizontal = 8:1. The mooring outline is included, together with schematics of internal tide characteristics (blue-dashed) from upper and lower slope and, in green, the spatial extent of internal wave breaking following a model by Winters (2015), see text. The insert shows the bathymetry from the 1'-version of Smith and Sandwell (1997), with the black dot indicating the mooring site. (b) Part of one fully packed drum shortly before deployment, with temperature (T)-sensors taped to a mooring cable and doubled in lanes between pins.

interior, only holds when near-boundary mixing is efficient (Garrett, 1990). This requires rapid transport of homogeneous waters into the interior and their replacement by stratified waters. This is not easily achieved by steady boundary layer flows as well-mixed, homogeneous waters have zero mixing efficiency. However, rapid restratification is induced by non-linear internal waves sloshing against a steep seafloor slope every wave period (Winters, 2015). Transport into the interior along isopycnals is accompanied by local small-scale shear-induced Kelvin-Helmholtz instabilities (KHi).

In this paper, high-resolution ocean temperature (T) observations are discussed from 760 T-sensors over a range of 1140 m above the sloping seafloor of large seamount Josephine NE-Atlantic Ocean. The moored observations are made to explore the range of turbulence due to breaking internal waves above sloping topography. Vertical and horizontal extents of internal wave breaking effects will be compared with detailed 2D numerical model results (Winters, 2015) of an internal tide moving up and down a slope. This model uses a vertical scale height of the buoyancy length $\delta = U_0/N$, where U_0 is a large velocity scale. This buoyancy length is dynamically important for turbulent motions. Winters' model results give an isopycnal excursion height of $\eta \approx 1.25\delta$, a vertical extent of turbulence from the seafloor in the breaker zone of $\Delta z = 4$–5δ and a lateral extent of small turbulent KHi away from the slope up to $\Delta y = 15\delta$. The present observations are from a site above Mount Josephine where locally enforced mean semidiurnal tidal amplitude $U_0 \approx 0.15$ m s^{-1}, $N \approx 1.5 \times 10^{-3}$ s^{-1}, so that $\delta \approx 100$ m. Following the numerical model, we expect turbulence due to breaking waves to extend away from the seafloor by about $\Delta z \approx 450$ m and $\Delta y \approx 1500$ m (Fig. 1). The latter value is close to L_{Roi} for a vertical scale of $h = 100$ m.

The paper is outlined as follows. In Section 2 technical details are given, including the custom-designed method to deploy 'KmT', the > 1 kilometer-long string of T-sensors. In Section 3 the observational results are presented including detailed time-vertical magnifications and extensive spectral analysis in various stages. Section 4 provides the discussion of the results and the embedding of the observations in general ideas of the impact of sloping topography on deep-ocean mixing and the extent thereof into the ocean-interior. In Section 5 conclusions are presented.

2. Technical details

KmT, an 1140-m long thermistor string array was deployed at 37°00′N, 013°44.5′W, with local seafloor at 2380 m waterdepth on the eastern flank of Mount Josephine (Fig. 1), about 400 km southwest of Lisbon (Portugal) on 25 April 2019 (yearday 114). It was recovered after 4 months on 26 August 2019 (yearday 237).

For the study on internal wave-turbulence from near to far above a sloping seafloor, 760 NIOZ4 high-resolution T-sensors were taped to the nylon-coated 0.006-m outer diameter steel cable and an inline-frame approximately halfway the cable. The T-sensors were at 1.5-m vertical intervals between 1233.5 and 2372 m. A 4.2-kN elliptic buoy was at 1105 m, 100 m above a similar second buoy holding a downward looking 75-kHz, 20° beam-slant angle to the vertical RDI/Teledyne Longranger acoustic Doppler current profiler (ADCP) (Fig. 1a).

The ADCP measures currents in three directions, $\mathbf{U} = [u, v, w]$ and relative acoustic echo intensity (dI) over a range of about 600 m. It houses tilt and pressure sensors. The ADCP was 20 m above the uppermost T-sensor of which the z-position approximately coincided with that of the ADCP's first vertical bin of useful data. The inline-frame held a second 75-kHz (deep-water version) downward looking ADCP to cover the lower 600-m range of the T-sensors (currents only). The ADCPs sampled at a rate of once per 900-s average values in 60 vertical bins of 10 m. The horizontal beam spread averaging of current components varied between about 15 and 420 m. Such scales of averaging are larger than the sizes of most turbulent overturning in the ocean.

In contrast, the 1.50 m vertically separated T-sensors sampled at a rate of once per 1 s with a sensor tip smaller than 0.001 m. Although the tip-size also resolves the smallest Kolmogorov scales of turbulence dissipation, the sensor-response time of about 0.5 s, the sampling rate and the vertical intervals between the T-sensors aim to resolve the most energetic turbulent overturning scales down to the Ozmidov scale L_O of stratified turbulence.

The mooring assembly was held tautly upright with net 5 kN buoyancy and the 8 kN bottom-weight generated net-anchoring with approximately 3 kN. The ADCPs tilt and pressure sensors demonstrated that even under maximum 0.3 m s^{-1} current-flow speeds the top of the mooring deflected little, vertically by < 0.2 m and horizontally by < 20 m. The mooring deflections are negligible compared with the vertical interval between the T-sensors and their positioning does not require correction during post-processing.

2.1. Site characteristics

The average local seafloor slope of $\gamma = 9 \pm 1°$ is scale-dependent. When computed using a 6-km horizontal scale, the larger scale slope is about 8°. When computed using a 2-km horizontal scale, local slopes go up to 10°. Seafloor slope criticality occurs when the slope to the horizontal of energy beams or characteristics of propagating internal waves matches that of γ. As propagating internal wave frequencies (σ) are generally found in the band 'IWB' $f \leq \sigma \leq N$, $N >> f$, their beam-slopes β depend on local f, N and σ: $\beta = \sin^{-1}((\sigma^2 - f^2)^{1/2}/(N^2 - f^2)^{1/2})$, e.g., LeBlond and Mysak (1978). A seafloor slope is supercritical when $\gamma > \beta$, steeper than the internal wave slopes of interest. A seafloor slope is subcritical when $\beta > \gamma$.

At the mooring site, $\gamma >> \beta_{M2} = 3.5 \pm 1.5°$ for dominant semidiurnal lunar M_2 internal tide characteristics (Fig. 1) under mean local stratification conditions resulting in $N = 1.8 \pm 0.6 \times 10^{-3}$ s^{-1}. The site is therefore considered supercritical for freely propagating internal tidal waves. Over the > 1 km vertical range of T-sensors, the wave-slope characteristics vary by a factor of 1.8, due to the vertical decrease in mean stratification (outside large-turbulence zones just above topography) with depth. In the interior, characteristics generally slope steeper at greater depths. Hypothetically, for example, for the intermediate depth-range between 1600 and 1800 m, propagating waves reaching the mooring line in that interval originate either from 1300 to 1500 m or from 1900 to 2050 m on the seamount slope (Fig. 1a). For comparison, the modeled horizontal extent of breaking internal wave turbulence above a

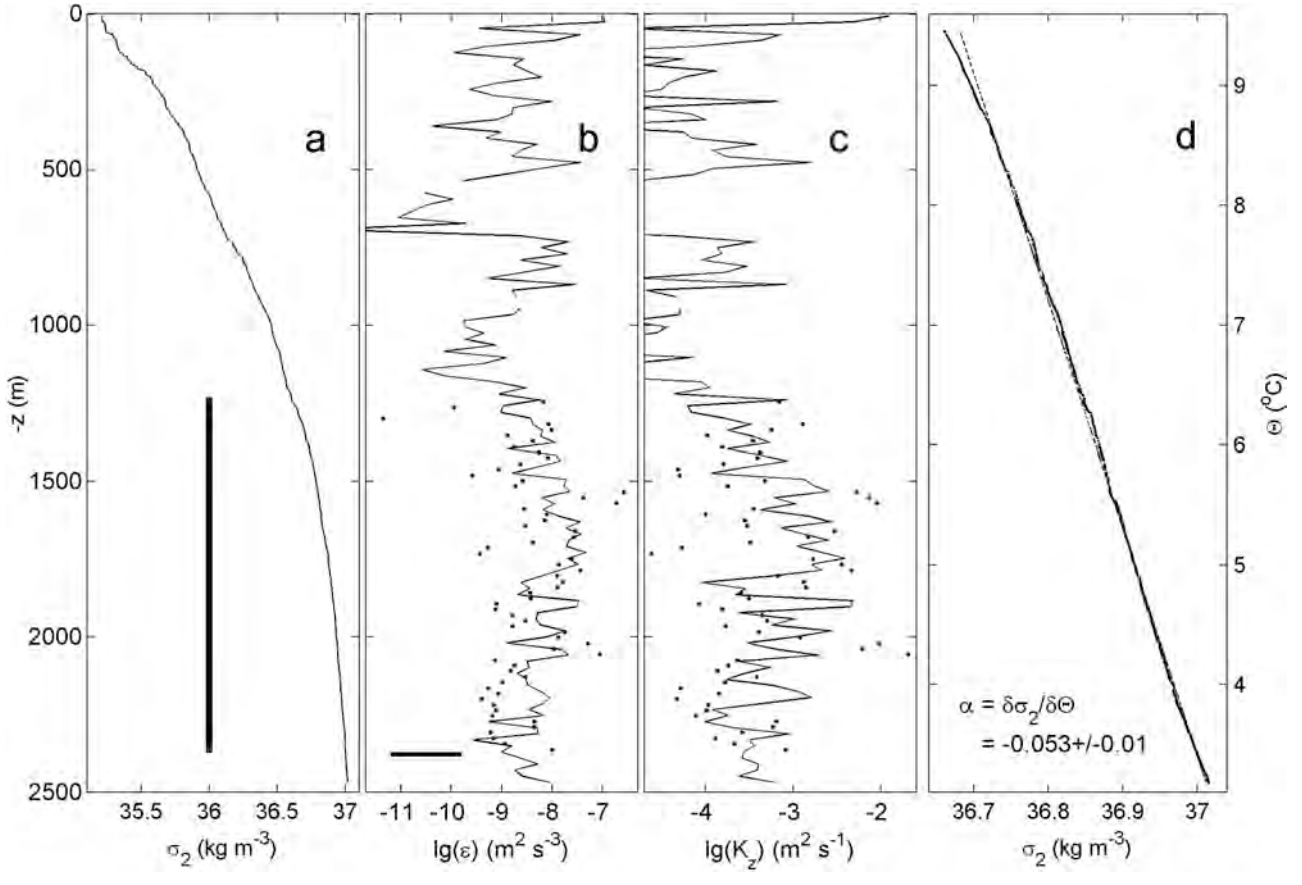

Fig. 2. Shipborne CTD-observations obtained on the day of deployment, obtained < 1 km horizontally from the mooring. (a) Potential density anomaly which is referenced to 2×10^7 N m^{-2}. Data are averaged in 0.33-m vertical bins. The vertical bar indicates the range of moored T-sensors. (b) Logarithm of turbulence dissipation rate computed from the sorting of a. (Thorpe, 1977) and averaged in 20-m vertical bins. The dots indicate 0.5-h and 20-m averages from the moored T-sensors around the time of CTD-lowering. The horizontal bar indicates the seafloor level at the mooring. (c) As b., but for eddy diffusivity. (d) Conservative Temperature – density anomaly relationship with linear best-fit slope (dashed line) for the range of moored T-observations.

supercritical slope reaches about 1 km horizontally from the slope (Winters, 2015). This breaking potentially does not reach the mooring line in the intermediate depth-range. Breaking is expected to only reach the mooring in the lower range from about 2200 to 2380 m on the seamount slope (Fig. 1a).

The top of the mooring and the uppermost sensors were about 120 and 240 m below the crest of the nearest ridge at 980 m waterdepth, respectively. The ridge is part of nearest sub-summit at 800-m waterdepth, about 14 km west-northwest of the mooring. Mount Josephine's absolute summit extends up to 250 m waterdepth. The top of the mooring reached into waters of the Mediterranean Sea outflow, potentially between about 1000 and 1400 m, so that partially salinity-compensated apparent density inversions were occasionally registered in the upper range of T-sensors when a Mediterranean outflow lens passed. Non-turbulence-induced artificial inversions are recognizable in the T-records as thin-layer instabilities lasting longer than a day. They can be distinguished from genuine turbulent overturning which are not expected to last longer than the inertial period (e.g., Dale et al., 2006). Mediterranean outflow intrusions are thus easily detectable and they are excluded from turbulence analyses.

2.2. Temperature sensors

NIOZ4 are self-contained T-sensors with a precision better than 5×10^{-4} °C after drift-correction, a drift of about 1×10^{-3} °C mo^{-1} after aging, and a noise level of $< 1 \times 10^{-4}$ °C (van Haren, 2018). Every 4 h, a synchronization pulse is sent via induction to all T-sensors of which the internal clock is adjusted to a single standard clock, so that the entire T-sensor range is sampled with less than 0.02 s delay between the sensors. In comparison with previous smaller moorings, the synchronizer for KmT is housed in a larger container holding twice the amount of batteries. The synchronizer is attached to the inline-frame, in the middle of the two T-sensor cable sections. The inline-frame is non-swiveled and attached directly via shackles to the mooring cables above and below, because the synchronization pulse is sent via flexible electrician's wire to the mooring cables. The wire is not to be cut by a potentially spinning frame. Two T-sensors are attached to the inline-frame and synchronized via the wire.

Although the synchronization was successfully used up to 400-m cable-length previously (van Haren, 2017), the present result for two sections of 510 and 630-m cable-lengths was unexpected as 93 out of 760 T-sensors showed difficulties in synchronization. A problem showed in the coating of the cable, which was scratched in some places causing electric leakage. But the range seemed the largest problem, as about 80 of the 93 failing synchronizations occurred at a distance of more than 400 m from the synchronizer. This distance is clearly the limit of the present electronics set-up for synchronization in seawater.

Failing synchronization is corrected by searching for the moment of acoustic mooring release upon recovery, which provides a time-stamp to within 1 s as the rather slim and heavily buoyant mooring ascents at a speed of about 1.3 m s^{-1}. The average correction to this time-stamp is 8 s over the 4-month record. The synchronizations to the time-stamp are interpolated over the entire 4-month record and implemented when they exceed half the (sub-)sampling interval for the portion of the record investigated. Some 53 T-sensors demonstrated electronics, data storage, battery, noise or calibration problems. The data from these sensors are linearly interpolated between those from neighboring T-sensors.

The T-sensor synchronization, together with the relatively small mooring deflections, implies a near-instantaneous and near-vertical 'synoptic' view of temperature over a range of 1140 m which is not achievable in standard moorings, via free-falling or lowered ship-borne instrumentation. An average advection speed of 0.1 m s^{-1} causes a horizontal mooring displacement of $\pm$ 1 m half-way the T-sensor array compared to the lowest and uppermost sensors, due to the 0.2°-tilt. Such displacement and tilt angles are more than a factor of 10 smaller than: 1/ The seafloor slope and associated bottom-normal coordinates in the lower 30 m of frictional influence above the sloping seafloor (Weatherly and Martin, 1978; MacCready and Rhines, 1991), 2/ sampling strategies like shipborne CTD or free-falling microstructure profiler (MP). The CTD- and MP-sampling takes 1200–1800 s to cross the range of moored T-sensors at standard vertical speeds by which structures measured at the depth of the uppermost T-sensor have been displaced horizontally by up to 1 km compared with those measured at the lowest T-sensor.

2.3. Deployment procedure

For a fully controlled deployment, the 1140-m long T-sensor cable is spooled in sections on two specially designed and custom-made 1400-pin drums (Fig. 1b). The drums have a diameter of 1.6 m for gentle curving of the mooring cable with attached 0.18-m long T-sensors. The pins enable to separate mooring cable and T-sensors in different lanes. Originally designed to contain approximately 250 T-sensors and up to 400 m of cable, the drums are used for KmT by doubling T-sensors in lanes. A short-cut wire was used between the brass anodes and the housing of the synchronizer to maintain the synchronization of the T-sensors whilst on the drums. A video of the spooling into the ocean during deployment can be found here: https://www.youtube.com/watch?v=QjhaIOifBsM.

2.4. Post-processing

The T-data are converted into 'Conservative' (~ potential) Temperature data Θ (IOC et al., 2010). They are used as tracer for density anomaly variations following the relation $\delta\sigma_2 = \alpha\delta\Theta$, $\alpha = -0.053 \pm 0.01$ kg m^{-3} $°C^{-1}$ (Fig. 2), where α denotes the linear coefficient under local conditions and subscript 2 indicates the reference pressure level of 2×10^7 N m^{-2}. This relation is established from data between 1250 and 2400 m of a shipborne CTD-profile that is obtained within 1 km from the mooring site.

Thus, given the reasonably tight density-temperature relationship, the number of T-sensors and their vertical spacing of 1.5 m, in combination with their low noise level, allows to calculate turbulence values like dissipation rate ε and vertical eddy diffusivity K_z via the reordering of unstable overturns (Thorpe, 1977). These overturns follow after reordering every 1 s the 1140-m high potential

density (Conservative Temperature) profile $\sigma_2(z)$, which may contain inversions, into a stable monotonic profile $\sigma_2(z_s)$ without inversions. After comparing observed and reordered profiles, displacements $d = \min(|z\text{-}z_s|)\cdot\mathrm{sgn}(z\text{-}z_s)$ are calculated necessary to generate the reordered stable profile. Certain tests apply to disregard apparent displacements associated with instrumental noise and post-calibration errors (Galbraith and Kelley, 1996). Such a test-threshold is very low for NIOZ T-sensor data, $< 5 \times 10^{-4}$ °C. Then, using d rather than its rout-mean-square (rms) value as explained in the paragraphs below,

$$\varepsilon = 0.64 d^2 N^3, \tag{1}$$

the turbulence dissipation rate, where N denotes the buoyancy frequency computed from each of the reordered, essentially statically stable, vertical density profiles. The numerical constant follows from empirically relating the rms-overturning scale $d_{rms} = (1/n\Sigma d^2)^{0.5}$ over n samples with rms-$L_O = (\varepsilon/N^3)_{rms} = 0.8 d_{rms}$ (Dillon, 1982). The value of 0.8 is thus an average over many realizations of the ratio L_O/d_{rms} distributed over at least one order of magnitude. Its use in (1) for moored T-sensor data is elaborated below. Using a constant mixing efficiency of $\Gamma = 0.2$ after substantial and suitable averaging (Osborn, 1980; Oakey, 1982; van Haren, 2017; Gregg et al., 2018), the turbulent eddy diffusivity is computed as,

$$K_z = \Gamma \varepsilon N^{-2}. \tag{2}$$

In (1), and thus (2), we use individual d to replace overturning scales, rather than taking their rms-value across a single overturn as originally proposed by Thorpe (1977). The reason is that we cannot easily distinguish individual overturns, first, because overturns are found at various scales with small ones overprinting larger overturns, precisely as one expects from turbulence, and, second, because some exceed the range of T-sensors.

Instead, we first calculate non-averaged d in (1) for high-resolution time-vertical images of $\varepsilon(t, z)$. Subsequently, we calculate 'mean' turbulence values by arithmetic averaging in the vertical [...] or in time <...>, or both. In order to compute average buoyancy frequencies, stratification rates N^2 are averaged before the square root is taken. Mean eddy diffusivities are computed by averaging heat fluxes, before computing mean K_z. (This yields average values which are about a factor of 2 lower than if one would use d_{rms} and mean N, both arithmetic operations over the entire vertical range, in (1).) Arithmetic averaging is mandatory over the vertical overturning scales to represent proper turbulence dissipation rates. Although turbulence dissipation rates are not normally distributed, arithmetic averaging is also used for time averaging, for consistency. Geometric time averaging following arithmetic vertical averaging would provide a factor of 1.5–2 lower mean values than presented in this paper. We note that this discrepancy is still within the error range, see next paragraph. The small discrepancy between geometric and arithmetic time averaged values may be because ocean turbulence temperature variance and dissipation rate are not necessarily log-normally distributed due to intermittency and multiple non-linear sources (Cimatoribus and van Haren, 2015; Cael and Mashayek, 2021). The 1-Hz sampling of moored T-sensor profile data allows sufficient averaging over all different turbulence characteristics.

The errors in the mean turbulence values thus obtained depend on the error in N and on the error in the temperature-density relationship, while the instrumental noise error of the T-sensors is negligible. Given the errors, the estimated uncertainty in time-vertical mean estimates of dissipation rate is about a factor of two, which gives the minimum error-range for turbulence values (Oakey, 1982). Presently, it is impossible to try better in natural waters where turbulence values from individual overturns vary over four orders of magnitude (e.g., Oakey, 1982; van Haren and Gostiaux, 2012; Gregg et al., 2018). Using similar T-sensor data from Great Meteor Seamount, van Haren and Gostiaux (2012) found turbulence values to within a factor of three similar to those inferred from ship-borne CTD/LADCP profiler data using a shear/strain parameterization near the seafloor. Their values compare well with profiler-based estimates in similar sloping topography areas by Klymak et al. (2008).

It has been argued that L_O/d_{rms} varies as a function of stratification, stage and type of turbulence generation (e.g., Chalamalla and Sarkar, 2015; Mater et al., 2015). While this seems acknowledged for specific unique conditions like pure convection and/or low Reynolds number flows, there are several reasons why it may not apply, and cannot be applied, to the present ocean data, as partially outlined in van Haren (2017) and summarized hereafter.

The moored high-resolution T-sensor data provide every second a 1140-m tall profile of temperature and thereby a priori insight in particular internal wave turbulence processes. However, we are not primarily concerned with individual overturning values. Instead we give "suitably averaged" turbulence values, as detailed below. In any given high Reynolds number environment like the deep ocean, shear- and buoyancy(convection)-driven turbulence intermingle and are difficult to separate. Examples of numerical modeling studies of particular stages of instability developments show that a finger of convective instability develops secondary shear instability along its fringes (Li and Li, 2006), while the roll-up stage of shear instability develops secondary convective instability mushrooms (Matsumoto and Hoshino, 2004). Comparison between calculated turbulence values using shear measurements and using overturning scales with $L_O/d_{rms} = 0.8$ from areas with such mixtures of turbulence development above sloping topography led to 'consistent results' (Nash et al., 2007), after suitable averaging over the buoyancy scales. Thus, from the argumentation above and the reasoning in Mater et al. (2015), internal wave breaking unlikely biases turbulence dissipation rates computed from overturning scales by more than a factor of two to three, provided some suitable time-space averaging is done instead of considering single profiles. This is within the range of our error.

3. Observational results

The shipborne CTD-data, obtained on the same day just after mooring deployment, demonstrate the common NE-Atlantic hydrographic situation including a decreasing potential density anomaly gradient with depth (Fig. 2a). The density variations are

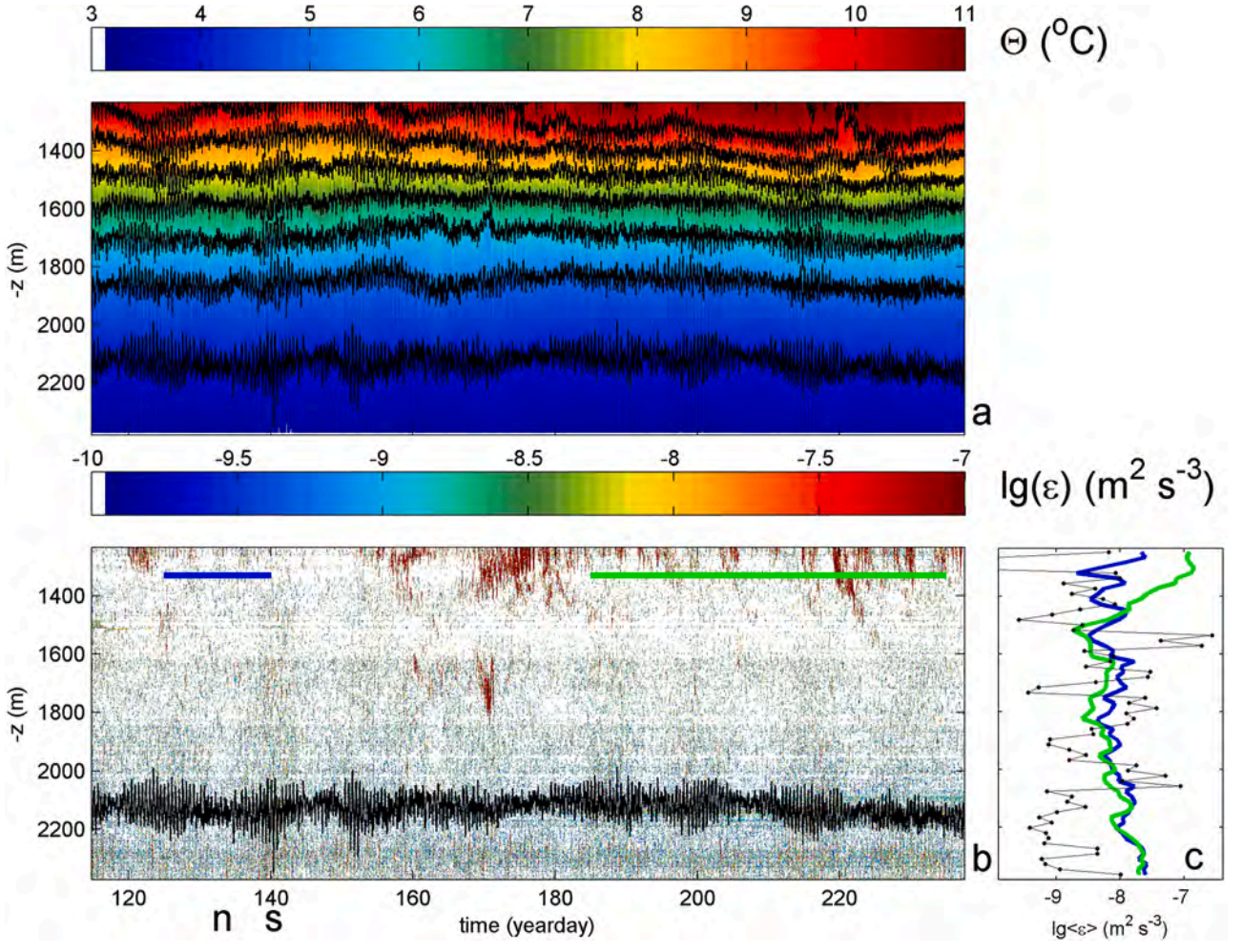

Fig. 3. Four-months, 1140-m overview of moored T-sensor data subsampled at once per 15 min and only generally corrected for instrument bias. (a) Conservative Temperature with black contours drawn every 1 °C. The x-axis is at the level of the local seafloor. (b) Logarithm of non-averaged turbulence dissipation rate. The 4 °C-contour is repeated from a. for reference. The two letters at the bottom indicate n(eap-) and s(pring-tide), example periods studied in more detail in Section 3. The color bars indicate averaging periods of c. (c) Logarithm of time and 20-m averaged turbulence dissipation rate for periods between days 125 and 140 (blue) and between days 185 and 235 (green), compared with the 0.5-h and 20-m average data from Fig. 2b.

dominated by temperature over salinity variations, which both decrease with depth. As a result, the temperature-density relationship demonstrates a slope-magnitude of $< |0.2|$ (Fig. 2d), but is otherwise fairly tight and linear (except when a Mediterranean outflow core is passing and salinity increases with depth over the range between 1000 and 1400 m, approximately). As an indication, rough calculations of turbulence values from the single CTD-profile compare reasonably well with those from 0.5-h-averages calculated from moored T-sensor data at the time of CTD-lowering (Fig. 2b,c). Both demonstrate generally larger turbulence values between 1500 and 2000 m, within the range of the T-sensors, compared to parts of < 1200 m. The CTD-profile provides a snapshot of data, as will be demonstrated from the moored T-sensor data subsequently.

3.1. Overview of mooring data

In the 4-month/1146 m time/depth overview plot of Conservative Temperature in Fig. 3a, generally warmer waters are observed above cooler waters thereby providing stable density stratification. With time, spring-neap cycles are seen in isotherm excursions. Strongest spring-tide values occur near the seafloor (e.g., around day 140). During this period, crest-trough variations of > 200 m are observed near the seafloor, like previously observed above a Hawaiian seamount slope (Levine and Boyd, 2006; Aucan et al., 2006) and above Mount Josephine slightly higher up the slope (van Haren, 2017). The baroclinic internal wave spring-neap modulations are not as deterministic as for barotropic surface (elevation) tides and vary considerably in time and in the vertical (Fig. 3a).

Additional warming is seen near the top of the T-sensor range mainly after day 150. This warming is indicative of passage of the

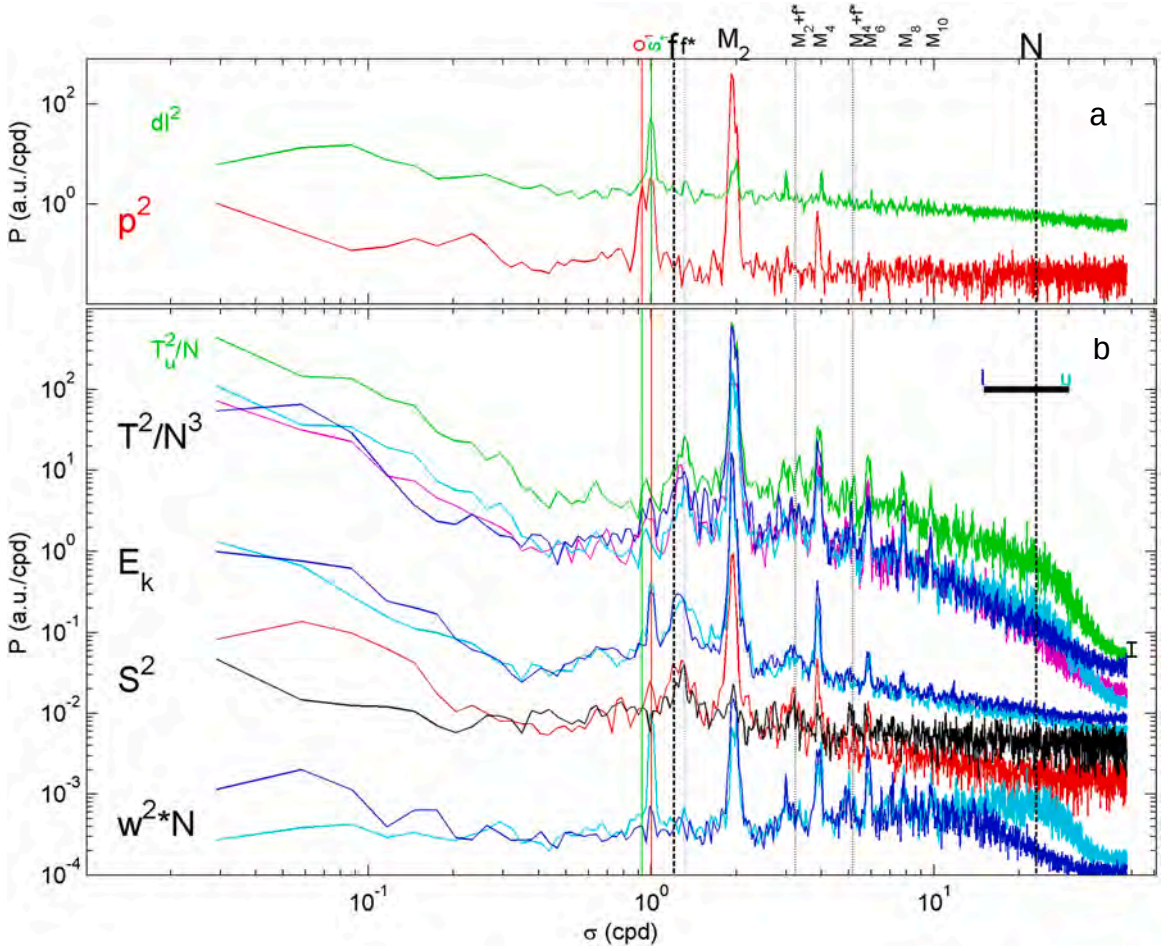

Fig. 4. Four-months and 150-m mean spectra from ADCP and T-sensor data (sub)sampled at once per 15 min. Data from u(pper) layer, between 1450 and 1600 m in which salinity-compensated layers are relatively few (see Fig. 3b and text), and l(ower) layer, between 2168 and 2318 m (1968 and 2118 m for currents see text), are shown in light- and dark-blue, respectively. (a) Relative echo intensity (dI; green) data from u and pressure data from upper ADCP (red) are given for reference of data in b. Spectra are arbitrarily shifted along the y-axis. Several frequencies are indicated, including lunar tidal harmonics M_x, x even, inertial f, near-inertial f* (see text) and 100-m-scale buoyancy N frequencies. (b) Temperature, current and shear spectra. The T-variance is scaled by local N^3, also for middle layer between 2000 and 2150 m (purple), and by N^1 (upper layer only; T_u, green), kinetic energy (E_k), mid-range 50-m-scale shear (S; black), 650-m S (red), and vertical current variance, scaled by local N^{-1}, are arbitrarily shifted along the y-axis per group. The horizontal bar of N indicates the range of mean values between l and u.

lower part of Mediterranean outflow waters with subsequent (unknown) salinity compensations and non-turbulent large dissipation rate values in Fig. 3b. The Mediterranean outflow reaches occasionally down to around 1500 m, on day 220. The high dissipation rate values between 1600 and 1800 m around day 170 are due to anomalously cooler temperature, see the associated upward isotherm motion in Fig. 3a, which must be compensated by relatively fresher waters of smaller salinity for stability and is thus not originating from the Mediterranean. Even more than in temperature, the time-vertical overview of dissipation rate in Fig. 3b does not show an obvious spring-neap cycle, as is expected from turbulence dominated by baroclinic internal wave breaking. Differences between spring and neap tide will become apparent in magnification plots below.

In Fig. 3c, time-mean turbulence dissipation rate values are about half an order of magnitude smaller than observed in a similar 400-m tall mooring just upslope above 1890-m waterdepth in 2015 (van Haren, 2017). In those previous observations, largest mean values were just above the seafloor and decreased only one order of magnitude over the 400-m range, as in the present observations. However, in Fig. 3c one sees that higher-up away from the seafloor $<\mathcal{M}>$ does not further diminish. Instead, a rather persistent 200-m banding is seen, e.g. with relatively high values between 1600 and 1800 m when the data around day 170 are excluded. Largest values are found near the seafloor as before (the 0.5-h during CTD-lowering was an exception with little activity in the lower 200 m above the seafloor) and around 1300 m. Such 1300-m turbulence values are artificial and associated with the Mediterranean outflow and do not appear in the data from the first month of deployment. Minimum mean turbulence values are observed around 1500 m.

Spectral overviews are computed for an u(pper) layer of 150 m between 1450 and 1600 m and for a l(ower) layer between 2168 and 2318 m. The u represents the interior stratification well away from the seamount and is least affected by anomalous warm or cold water. The deepest value of l is determined by theoretically good non-sidelobe-affected mid-line ADCP-data. Practically, the amount of acoustic scatterers was limited at great depths, so that non-contaminated spectra for current and acoustic echo data are computed for a range between 1968 and 2118 m. Spectra are averaged for all data within these vertical ranges, except for 50-m-scale shear S, and over the entire 4-month deployment for Fig. 4.

The barotropic, vertically homogeneous surface tide is small in temperature and current data which are dominated by baroclinic, vertically varying internal waves. Common methods to remove the barotropic tide from time series data for internal wave studies are small-width band-pass filtering each time series using 'harmonic analysis' to remove deterministic signals and vertical data averaging. Both methods have a disadvantage, because harmonic analysis also removes some of the baroclinic signal and the vertical range of observations is covering only half instead of the entire water depth. For the present open-ocean data, spectra are computed without applying these methods because barotropic motions are negligible compared to baroclinic motions.

To verify the limited barotropic tide, spectra are compared with that of upper ADCP's pressure data which are dominated by the surface tide (Fig. 4a). The p-record shows sharp peaks at diurnal tidal O_1 and K_1 (indistinguishable from solar S_1), semidiurnal N_2 (barely visible in Fig. 4a), M_2, S_2, and fourth diurnal M_4. The diurnal frequencies are sub-inertial, outside IWB and cannot represent freely propagating internal waves. Also in Fig. 4a, the dI-spectrum averaged over u is given for reference of diurnal solar S_1 deep plankton migrations. This record shows a sequence of higher harmonic peaks at S_2, …, S_8 that reflects a block-signal common in plankton migration (van Haren, 2007). Also for reference, shear (vertical current differences) are computed over large 650-m vertical scales and presented in Fig. 4b. Outside frictional boundary layers, barotropic motions are vertically homogeneous and thus do not generate shear. However, the 650-m vertical shear shows a strong semidiurnal tidal peak which extends above the spectral continuum as far as that of kinetic energy semidiurnal tidal peaks. This suggests a strong amplitude or phase vertical variation in the tidal motions, like in a baroclinic tide. Barotropic, vertically homogeneous tides are also not distinguished in time-vertical magnification plots below, which are dominated by vertical variations in magnitude and/or phase of all variables. By nature, temperature data show negligible barotropic tide because, outside fronts, isotherm-excursions are O(100) times larger than surface tidal displacements and because their spectra show no peaks at diurnal tidal frequencies. In currents, notably vertical, a peak is visible at S_1, caused by plankton motions.

Large tidal spectral peaks thus reflect large vertical scales of baroclinic motions rather than barotropic motions. Peaks of lesser value in the spectra, such as between 1.4 and 3.4 cpd (short for cycles per day; 1 cpd = 1/13751 s^{-1}), also evidence internal wave (interaction) motions instead of barotropic motions. The major motions are discussed below.

The N-range established from CTD-observations over the extent of T-sensors in 100-m vertical intervals corresponds well with the spectral humps in w-variance and the roll-off in T-variance, especially in u. Local N, which varies by a factor of 2 between l and u, also scales the T-variance at M_2 almost perfectly, but not at any other frequency (σ) although near-scaling to within statistical significance is found at M_4 and the turbulence-Nyquist frequencies. Generally, N-scaled T-variance of u exceeds that of l. This is not an effect of potential influence of salinity-compensated temperature anomalies, as these are excluded, and which confirms findings from the open Canary Basin (van Haren and Gostiaux, 2009).

Non-linearity is visible by the sequence of higher tidal and inertial-tidal harmonics in the T-variance spectral IWB [f, N] and suggests governance by the advection term in equations of motion and buoyancy. Most near-inertial motions show a blue-shift peak, except in w. The apparent near-inertial frequency $f^* = 1.083$ f. Here, it is assumed that $f^* = f + \varsigma/2$ equals the absolute vorticity and ς the relative vorticity induced by large-scale sub-inertial flows. Such flows are hypothesized to be related to (flow around) the seamount. Modeling shows that it may be persistent in the vicinity of the seamount (e.g., Perfect et al., 2018), possibly explaining the relatively sharp peaking at f*.

The f* is involved in a sequence of peaks at near-inertial/tidal interaction frequencies. The higher harmonics sequences stop around σ = 10 cpd. The sequence is less clearly extending above the spectral continuum in kinetic energy (E_k) compared to T-spectra, while more clearly in w-spectra. Compared with l, higher harmonics in u follow a more monotonic decrease with frequency. The reduced M_6-peak in lower range-T is out of sequence. Although inertial motions are smaller than expected, motions at inertial-tidal interaction frequencies are still distinguishable from odd tidal harmonics like $M_3 < 3$ cpd ($M_2 + f = 3.15$ cpd).

Although E_k is least resolved because of the relatively high noise levels of the ADCPs, all spectra show a sequence of peaks at higher

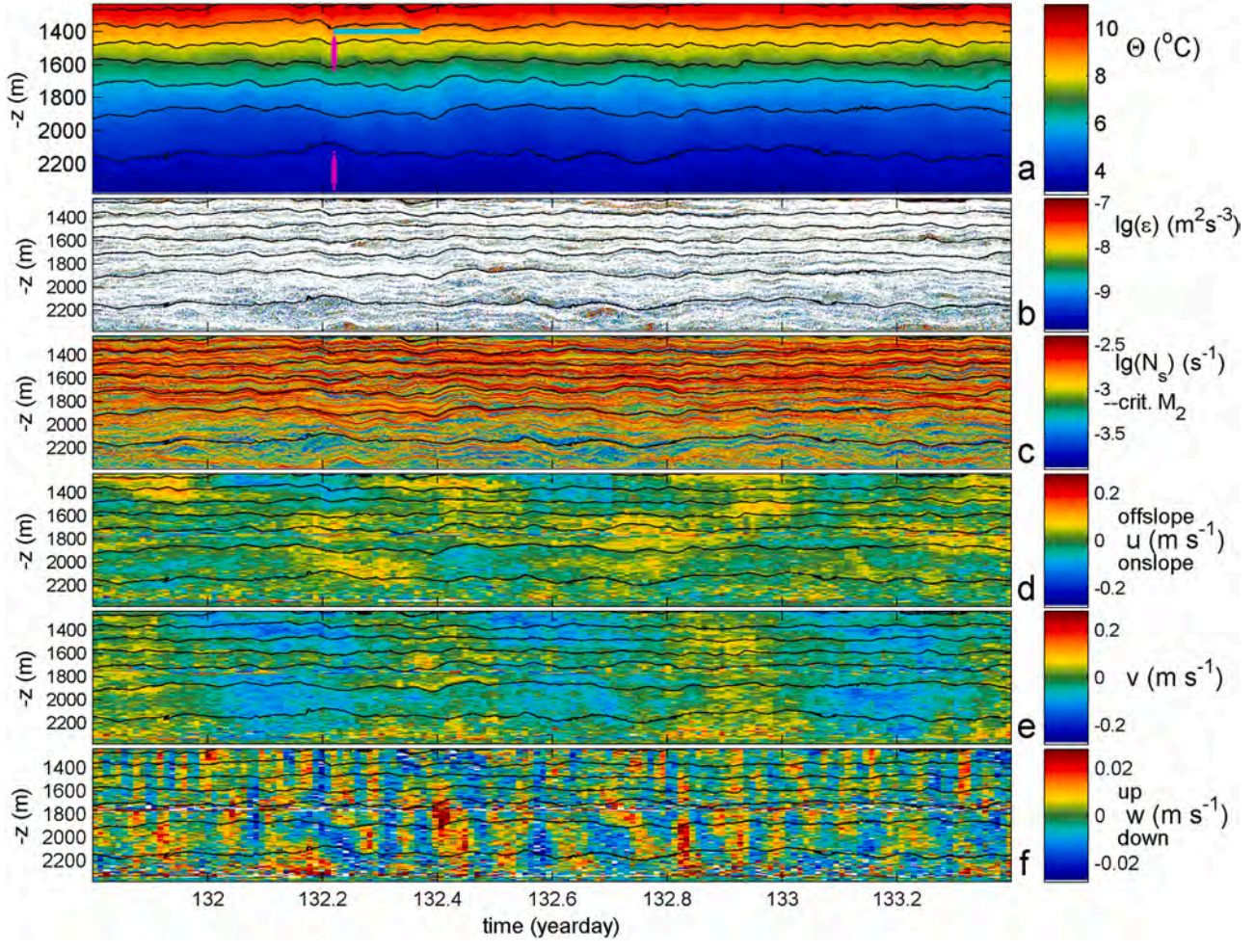

Fig. 5. Detail of two inertial and three semidiurnal lunar periods (totaling 1.6 days) around the second neap tide in the record. In all panels, the seafloor is at the level of the x-axis. (a) Conservative Temperature from T-sensor data sub-sampled at 0.1 Hz, with black contours at 1 °C intervals. These contours are repeated in all subsequent panels, for reference. The light-blue and magenta bars indicate the time range and upper and lower layers' vertical ranges of two detail plots in Fig. 7a,b, respectively. The thicker magenta parts indicate the 150-m ranges used to compute spectra in Figs. 4, 8 and 9. (b) Logarithm of non-averaged turbulence dissipation rate from the data in a. (c) Logarithm of 1.5-m-scale buoyancy frequency calculated from the vertically sorted version of a. (d) East(positive; offslope)-West(negative; onslope) horizontal current component from 900-s sampled, 10-m binned ADCP-data. (e) As d., but for North(positive)-South(negative) horizontal current component. (f) As d., but for up(positive)-down(negative) vertical current component. Note the different scale compared to d., e.

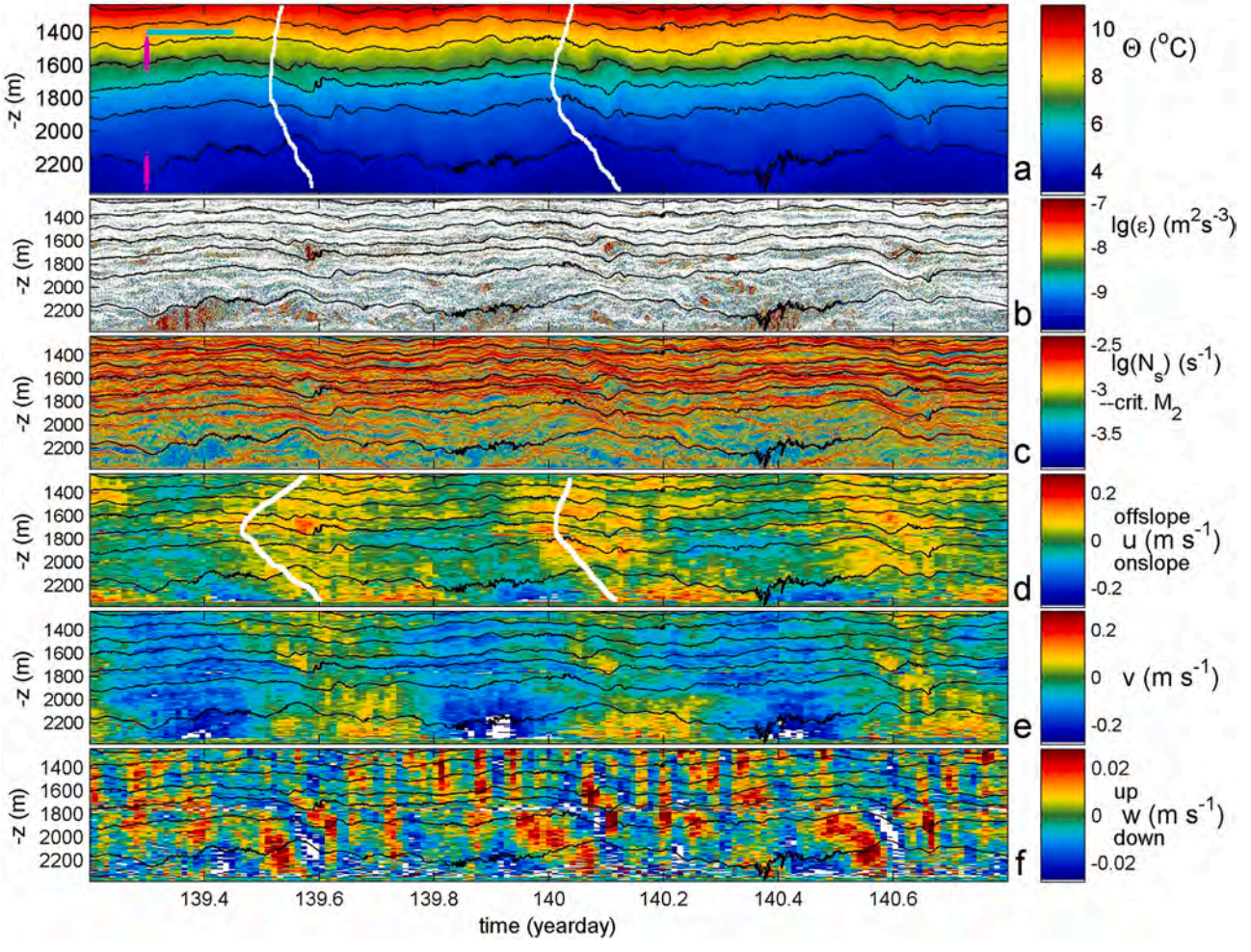

Fig. 6. As Fig. 5 with identical scales in all panels, but for the second spring tide in the record. The light-blue and magenta bars in a. indicate the time and vertical ranges of detail plots in Fig. 7c,d. The white lines indicate approximate co-phase lines.

tidal harmonic and, less pronounced, of inertial-tidal interaction frequencies (Fig. 4b). While the spectra look peaked-like, they are not exactly deterministic as the peaks' bandwidth is finite, extending over a range of about 10 % of the fundamental frequency between levels of 0.1 times their peak value (if extending above the spectral continuum). The E_k-peak at f is not very pronounced, which is expected for T- and w-variance but not for E_k. Advective motions at the diurnal frequency are not negligible. The present E_k-spectra do not scale with local N, and M_2 and M_4 show even larger (unscaled) E_k in l, with lower N, than in u. Apparently, there is an effect of the vertical distancing to sloping topography. The dominant peak of 50-m-scale shear is at f*, rather than at semidiurnal frequencies for the large 650-m-scale.

T-variance scales differently at various frequencies. At M_2, it scales like N, at f (and to lesser extent at M_4, M_8) like N^2, while for the rest of IWB, and also at most sub-inertial frequencies $\sigma < f$, T-variance scales like N^3. W-variance scaling is close to N^{-1}, at all $\sigma < 10$ cpd, except at the diurnal frequency. This N^{-1}-scaling for w^2 is anticipated for equilibrium internal waves and associates with the N^3-scaling for T^2, because $w^2 \propto \eta^2 \propto (T/(dT/dz))^2 = T^2N^{-4}$, where η denotes vertical isotherm displacements (Krauss, 1966; Munk, 1981).

From an internal wave point of view, the inconsistency between N-scalings of T- and w-variance at M_2 (and some higher harmonics) may be related to the different sampling (scales), as w is sampled by ADCPs on large scales only. However, this would favor correct scaling at M_2, because the largest internal wave scales occur at that frequency. This is confirmed by comparing an N^3-scaled spectrum from a middle layer between 2000 and 2150 m with the N^3-scaled T-variance in u. Both compare reasonably well also at M_2, with some remaining discrepancies at higher harmonics. The N^3-scaled middle layer T-variance departs from that of the N^3-scaled l at 19 cpd, which is the middle layer mean N-value.

Evidently, T_{M2} in l is elevated with respect to the IWB-scaling, like E_k, even though internal tides do not reflect off a critical slope for given local mean N. However, the local slope is critical if the buoyancy frequency were equal to 10 ± 1 cpd, at which frequency scaled T-variance in u departs from spectra in the other two layers. Alternatively, the internal tide may be non-linearly reinforced by the steep slope, which could also explain the elevated levels at several higher tidal harmonics. This results in bound not-freely-propagating motions. The high-frequency end of the non-linear higher harmonics sequence at $M_{10} \approx 6f_h$ could be explained by local (minimum) stratification, not the absolute minimum. This local minimum stratification may absorb some of the energy into propagating internal waves, see the relatively wide frequency-range of the N-bulge in w-spectrum of u (Fig. 4b). Or, it is overprinted by turbulent overturns extending the turbulence inertial subrange. This will be elaborated with extended spectral analysis in Section 3.4.

3.2. Details in time-vertical magnifications

A magnification plot shows the typical ocean unrest also during neap tide, with moderate internal wave activity and no clear tidal periodicity in temperature (isotherm-excursion) variations (Fig. 5a). Nevertheless, turbulent overturning occurs regularly, to the extent that the 1.6-d, 1140-m mean $[<\varepsilon>] = 7 \pm 4 \times 10^{-9}\ m^2\ s^{-3}$, $[<K_z>] = 4 \pm 2 \times 10^{-4}\ m^2\ s^{-1}$, $[<N>] = 1.8 \pm 0.2 \times 10^{-3}\ s^{-1}$. Lower 100/150-m mean values are: $[<\varepsilon>] = 1.4/1.2 \pm 0.6 \times 10^{-8}\ m^2\ s^{-3}$, $[<K_z>] = 2.0/1.7 \pm 0.5 \times 10^{-3}\ m^2\ s^{-1}$, $[<N>] = 1.2/1.2 \pm 0.2 \times 10^{-3}\ s^{-1}$. The turbulent spots alternate with blank areas throughout the t,z-image (Fig. 5b). Near the top of the image a few turbulent spots around days 132.4, 132.8 and 133.3 are possibly artificial and attributable to intrusions of partially salinity-compensated layering. Otherwise, no clear Mediterranean outflow effects are observed. More intense turbulent overturning generally associates with less stratification. Such spots are generally more abundant near the seafloor than higher up (Fig. 5c). In this plot of (logarithm of) 1.5-m-scale buoyancy frequency N_s from sorted T-data, thin-layering is manifest and constant N does not exist. If $\lg(N_s) = -3.14$ ($N_s = 7.2 \times 10^{-4}\ s^{-1}$) throughout, the seafloor slope would critically match the slope of M_2-internal tide characteristics. Up in the range, stratification becomes larger with thinner near-homogeneous layers. Thin strongly stratified layers seem to follow isotherms, but seldom longer than one inertial period as is verified after careful inspection.

Thin-layering, as opposed to constant vertical density stratification, also affects the current components, although these are much coarser sampled than temperature. While the horizontal components [u, v] (Fig. 5d,e) demonstrate dominant semidiurnal periodicity, they are overprinted with smaller-scale variations that associate with the density/temperature thin-layering, in the vertical as well as in time. Thus, locally largest amplitudes are found in thin-layers like around 1400 m and day 131.9, whilst the largest v-component shows semidiurnal periodic peaks near the seafloor. The layering in tidally dominant u and v is reminiscent of patchiness observed in internal tidal wave beams emanating from a continental slope and in near-horizontal patchy layering off a (different) seamount (van Haren et al., 2010). The patchy layering could be traced 20–30 km horizontally from the sloping topography.

In contrast, the t,z-image of vertical current component is dominated by high-frequency internal wave motions near N. These alternating up- and downward motions are coherent over several 100's of meters vertically, thereby extending over much larger distances than the horizontal thin-layering of typically 10–100 m. The vertical w-ranges are however also broken up in smaller portions, and sometimes are inclined in the t,z-plain, thereby reflecting interaction with the layered stratification.

Compared with the neap period in Fig. 5, the spring period in Fig. 6 is more intense in many ways. This increase in intensity only moderately shows in half an order of magnitude larger mean turbulence values, as 1.6-d and 1140-m mean $[<\varepsilon>] = 2.4 \pm 1 \times 10^{-8}\ m^2\ s^{-3}$, $[<K_z>] = 1.5 \pm 0.5 \times 10^{-3}\ m^2\ s^{-1}$, for $[<N>] = 1.8 \pm 0.2 \times 10^{-3}\ s^{-1}$, mean $[<N>]$ being the same as found during neap tide. Lower 100/150-m mean values are: mean $[<\varepsilon>] = 7.4/6.1 \pm 3 \times 10^{-8}\ m^2 s^{-3}$, $[<K_z>] = 9/8 \pm 4 \times 10^{-3}\ m^2\ s^{-1}$, for $[<N>] = 1.3/1.2 \pm 0.2 \times 10^{-3}\ s^{-1}$. For comparison, lower 150-m and 1-month mean values from 1890-m waterdepth above Mount Josephine gave: $[<\varepsilon>] = 2 \pm 0.5 \times 10^{-7}\ m^2\ s^{-3}$, $[<K_z>] = 8 \pm 3 \times 10^{-3}\ m^2\ s^{-1}$, for $[<N>] = 1.5 \pm 0.2 \times 10^{-3}\ s^{-1}$ (van Haren, 2017). 100-m and 1-month mean data from 2530-m waterdepth in 2015 gave: $[<\varepsilon>] = 2 \pm 0.5 \times 10^{-8}\ m^2\ s^{-3}$, $[<K_z>] = 7 \pm 3 \times 10^{-3}\ m^2\ s^{-1}$, for $[<N>] = 1.1 \pm 0.2 \times 10^{-3}\ s^{-1}$. The latter value is still significantly larger than the value of $7.2 \times 10^{-4}\ s^{-1}$ required to critically match the internal M_2-tidal characteristics. Thus, the slope remains super-critical for internal tides, except during brief periods that are much smaller than the tidal period.

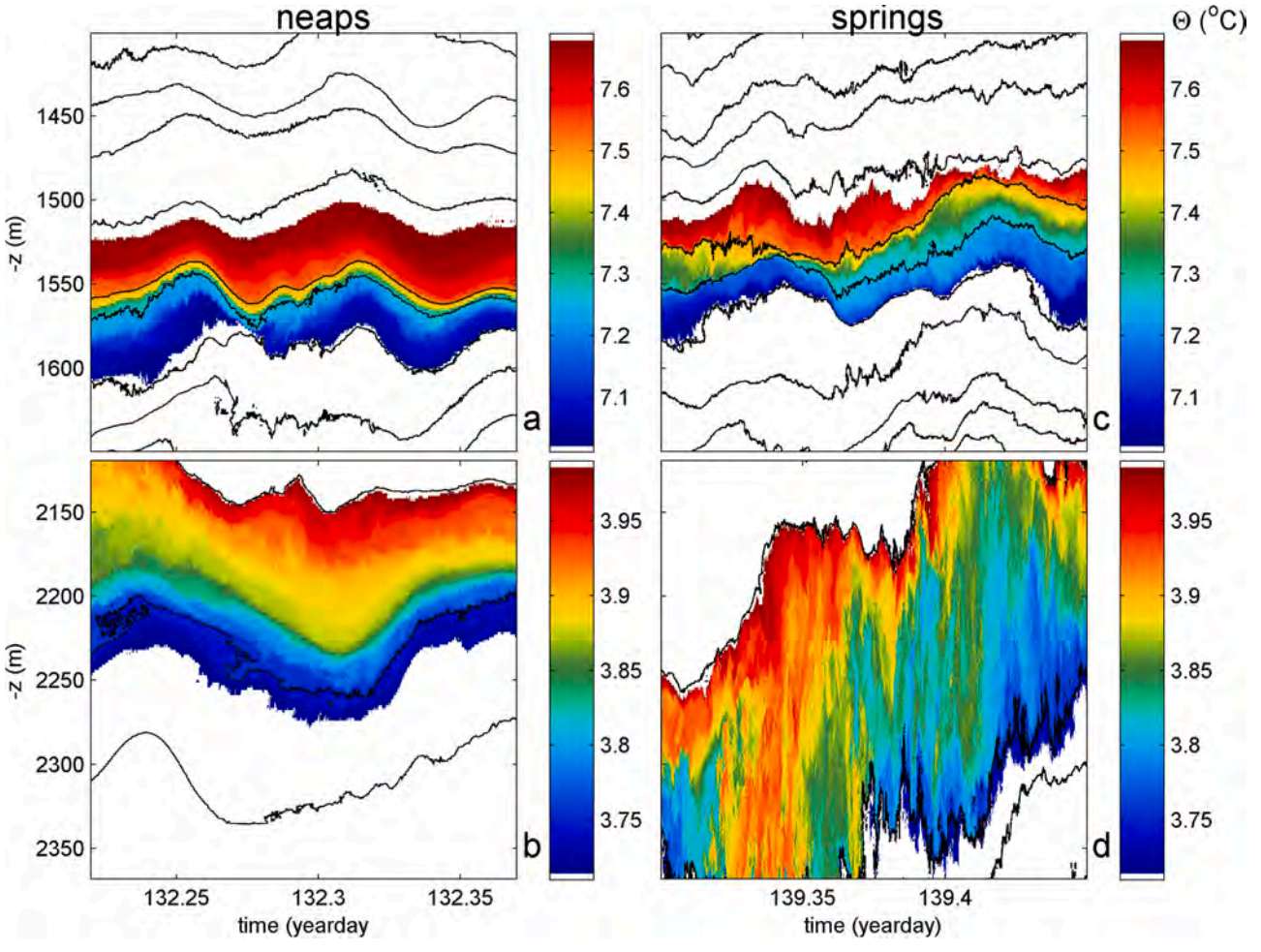

Fig. 7. 3.6-h, 250-m Magnifications of Conservative Temperature in Figs. 5a, 6a. The central 150 m of all ranges contain data that are spectrally analyzed in Figs. 9, 10 as u (a., c.) and l (b., d.). For both layers different color ranges are used to highlight characteristics. Isothermal contours are drawn in black every 0.25 °C. (a) Neap tide in u. (b) Neap tide in l. (c) Spring tide in u. (d) Spring tide in l.

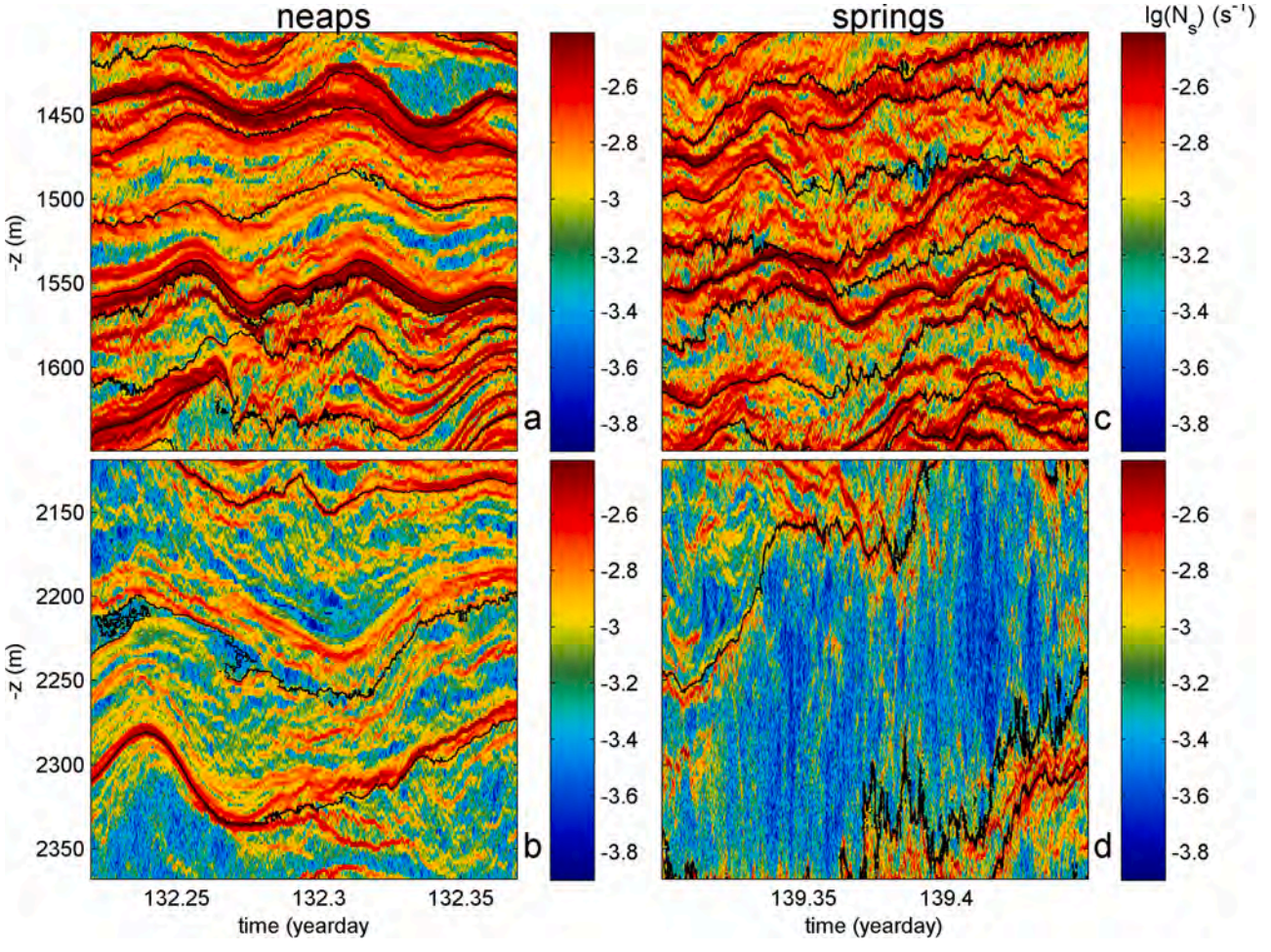

Fig. 8. As Fig. 7, but for logarithm of 1.5-m-scale buoyancy frequency calculated from vertically sorted Conservative Temperature data. The black contours are redrawn from Fig. 7, for reference.

Underlying these mean turbulence values, spring tide's increased variability in temperature shows as larger isotherm excursions that are also sometimes overprinted with intense small-scale variations appearing as thicker black isotherms (Fig. 6a). Semidiurnal variability is evident, with isotherm crest-trough variations peaking > 200 m in the lower half. In the upper half, semidiurnal excursions are also visible but these are not in phase with those near the seafloor. (The phase difference is about 100°, with downward phase propagation suggesting upward energy propagation in interpretation of freely propagating internal waves).

In the mid-range layer between 1600 and 1800 m apparent local mode-2 isotherm 180° out-of-phase excursions are visible at the same time or just after the peak in the lowest isotherm above the seafloor around days 139.6, 140.1 and 140.6. It is to be investigated whether these KHi in the interior are associated with the straining by the large semidiurnal waves near the seafloor. In Fig. 5a two such local mode-2 excursions were observable slightly deeper (around 1800 m), around days 132.75 and 133.4. These have hardly any effects in turbulent overturning and stratification. In Fig. 6b however, the interior mixing is clearly evident around the three times of local mode-2 isotherm excursions.

Although more turbulent patches seem visible in the interior than in Fig. 5b, largest turbulent overturns are found in the lower 100 m just above the seafloor, with three breaking events in Fig. 6b. They all result in locally (both in the vertical and in time) reduced stratification (Fig. 6c) and associate with the transition from off- to onslope phase of the lower isotherms and cross-slope current component (Fig. 6d). Thus, they potentially reflect upslope propagating turbulent frontal bores near the seafloor. They associate approximately in phase with a negative peak in v, southward flow (Fig. 6e).

Horizontal currents (Fig. 6d,e) are patchy and layered as in Fig. 5d,e, and generally have larger amplitudes, especially also near the seafloor, than in Fig. 5d,e. Also, strong vertical phase differences are observed, especially in u notably around day 139.5, with upward phase difference above 1600 m and downward phase difference below 1800 m. As freely propagating internal waves have opposite vertical directions for phase- and energy-propagation, this suggests a focusing of internal tidal energy between 1600 and 1800 m.

No clear association is found with upward motions during a frontal passage (Fig. 6f), although the high-frequency internal waves following a bore demonstrate w-disturbance reaching up to 1800 m (600 m above the seafloor). Higher up in the interior, the vertical internal wave motions also have larger amplitudes than in Fig. 5f. Once per tidal period, w shows a $|0.05|$ m s^{-1} spike extending up to 250 m above the seafloor just before the crest in the lower isotherm (Fig. 6f). Semidiurnal periodicity is dominant in this range. The strong vertical phase difference of up- and backward bending of one period of enhanced w-intensity is visible above each wave crest in l. This points at slow downward phase propagation. It reaches to the level and moment of initiation of the mid-range KHi.

3.3. Short-term magnifications

Further magnifications are selected for the neap- and spring tide images of Figs. 5, 6, under the subjective conditions that they are representative of their tidal period and that they cover u or l. At a first glance, spring tide confirms more turbulent overturning than during neap tide. This is evident in vertical irregularly colored motions, but also in more rugged, less smooth isotherms during spring tide than during neap tide. Weakest and smallest turbulent overturning with smoothest isotherms occurs in u during neap tide (Fig. 7a), whereas strongest and largest turbulent overturning is observed in l during spring tide (Fig. 7d). The largest number of isotherms is observed in u during spring tide (Fig. 7c). In the same period in l (Fig. 7d), > 100-m large overturns and ditto distancing between isotherms are observed.

However, the relatively smooth period of Fig. 7a still demonstrates sporadic turbulent overturning on smaller scales. While the neap tide detail of u shows typically 10-m overturns, as shear-induced 'hooks', e.g., around 1560 m (Fig. 7a), the neap tide detail of l shows 20–30-m overturns, e.g., around 2150 and 2230 m (Fig. 7b). Spring tide in u shows more pointed like instabilities of 10–20 m (Fig. 7c) that may appear less shear-induced than overturns during neap tide. Spring tide in l shows 100-m tall convective overturns (Fig. 7d). This is viewed from a different perspective in plots of logarithm of 1.5-m-scale buoyancy frequency (Fig. 8).

The variability in stratification highlights the continuous results of ocean turbulence and internal wave (straining) action. At all scales, stratification varies in intensity, with down to one-pixel-thin strongly stratified layers alternating with near-homogeneous layers more than 100-m thick. Also within the weaker stratified layers $\lg(N_s)$ is seen to vary on smaller scales, with short stronger stratified layers that are inclined at more acute angles from the vertical (e.g., Fig. 8a,c) and even near-vertical (Fig. 8d).

While isotherms generally follow the t,z-motions of strongly stratified layers by internal wave action, departures are noticeable in isotherms switching from one thin layer to another (e.g., Fig. 8a, 1500 m), and sometimes also back. This implies that internal modifications of (temperature-) stratification occur, as precise following of isotherms and thin-layer stratification indicates pure advective motions without internal modifications. In general, the thin-layers do not persist longer than one inertial period. This is different from open-ocean observations of intrusions of varying T-S water properties in layers around a warm-core ring well away from topography that can be traced for months (e.g., Schmitt, 1987). However, it is typical in near-surface waters in which layers last for several hours (Alford and Pinkel, 2000) up to the inertial period (Dale et al., 2006).

3.4. Internal wave-turbulence temperature spectral analysis

3.4.1. Four-month mean

Ocean spectral analysis includes evaluation of variance-content at particular frequencies in line-spectra, which represent 'narrowband' or 'deterministic' signals such as tides, and of content that is distributed over a certain range of frequencies representing 'broadband' signals. Broadband signals need not be purely stochastic, although these are often called 'noise' with a color (e.g., Schuster, 1984). They can also represent several non-linear interactions between motions at a limited number of parental (wave) frequencies, thereby showing an intermittent character to a degree. Large broadband, or spectral continuum, signals are commonly

characterized by spectral slopes with frequency σ^x, which are linear in a log-log plot. They include x = −2, − 5/3, − 7/5, − 1, and describe E_k of internal waves without tides (Garrett and Munk, 1972) as well as fine-structure contamination (Phillips, 1971), shear-induced turbulence inertial subrange for passive scalars (Ozmidov, 1965; Tennekes and Lumley, 1972; Warhaft, 2000), active scalar convective turbulence or the Bolgiano-Obukhov scaling (Bolgiano, 1959; Pawar and Arakeri, 2016), and open-ocean internal wave T-variance continuum (van Haren and Gostiaux, 2009) and intermittent pink noise signals describing deterministic chaos (Schuster, 1984), respectively.

Less clear are physical processes behind the filling of these broadband signals, e.g. non-linear interaction models. While the Kolmogorov turbulence model (Kolmogorov, 1941; Ozmidov, 1965) is a forward energy cascade model, the filling of the broadband signals from higher harmonic sequences needs to be established. Similarly, does a contribution of backwards cascading exist, e.g. from N to lower IWB-frequencies? Do non-linear waves remain bound to the parental source waves or can they propagate freely? Weakly non-linear resonant wave-wave interactions suggest energy-transfer from a range between 2f and 3f to lower and higher frequencies (e.g., McComas and Bretherton, 1977; Eden et al., 2019). However, a spectral gap has not been observed in that frequency range. This wave-wave interaction model does not describe higher tidal/inertial harmonics, for which a non-resonant strongly non-linear forced interaction model like a shock-wave model seems more adequate (Platzman, 1964; Phillips, 1977). In the detailing spectra below we cannot answer these questions, but we seek the interminglement of internal wave and turbulence transition.

In Fig. 9a, the four-month mean temperature variance spectra from u and l are presented for the IWB. Data are sub-sampled over 900 s for computational reasons and for comparison with Fig. 4. In contrast with Fig. 4, spectra are not scaled with (some power of) N but with the turbulence inertial subrange slope of $\sigma^{-5/3}$ for investigation of the transition from internal waves to turbulence.

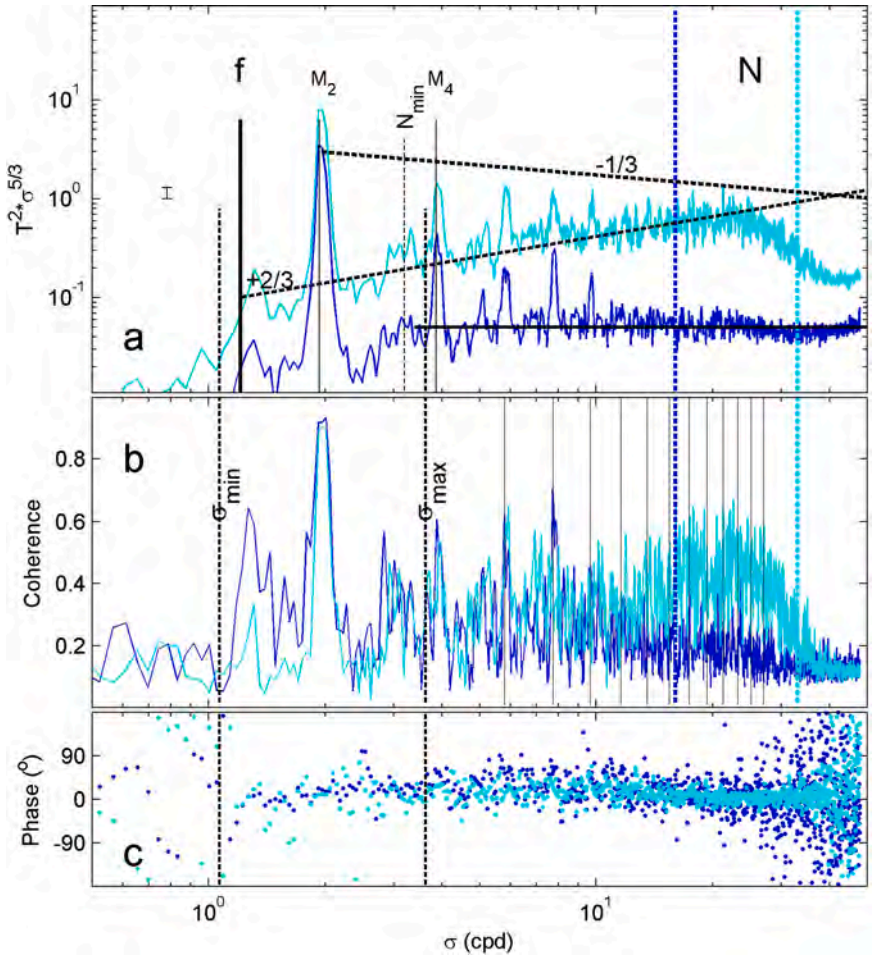

Fig. 9. Mean spectra for (light-blue) and l (blue) of 15-min subsampled 100 T-sensor data from Fig. 4. (a) Log-log plot of T-variance scaled with the turbulence inertial subrange slope − 5/3 (horizontal black line) and heavily smoothed (1600 dof, short for degrees of freedom). Vertical color lines indicate the associated mean 100-m-scale N. Vertical black lines indicate the minimum buoyancy frequency N_{min}, tidal M_2, M_4, and inertial f frequencies. The smaller thick-dashed lines indicate the inertio-gravity wave bounds [$\sigma_{min} < f$, $\sigma_{max} > N_{min}$] under (N_{min}) weakly stratified conditions. The sloping lines indicate several deviations from the inertial subrange (see text). (b) Associated coherence for data from a. between all possible pairs of T-sensors separated over 100-m vertical scales. The 95 % significance level is approximately at coh = 0.15. (c) Phase associated with b.

Larger variance is found at all frequencies in u compared to l. Ignoring the higher harmonics peaks, the spectral continuum in u is characterized by a + 2/3 slope, i.e. a − 1 slope in an unscaled log-log plot, for the range [f, 0.7N].

In contrast in l, most of the IWB-continuum in the range [$N_{min} = 2f_h \approx M_2 + f^*$, $\sigma_{Nyq} >> N$], where $f_h = 2\Omega\cos\varphi$ denotes the horizontal Coriolis parameter and σ_{Nyq} the Nyquist frequency, shows a flat 0-slope, i.e. − 5/3 in an unscaled log-log plot. This represents a mean dominant inertial subrange of shear-induced turbulence, which thus penetrates well into the IWB across the range [N_{min}, N]. This turbulence-inertial-subrange penetration in the IWB seems at odds with the duration of near-homogeneous patches and layers of which the largest last 1.5–2.5 h. These durations correspond with the periods of N and $M_{10} \approx 6f_h \approx 10$ cpd, respectively. For $\sigma > 6\ f_h$, no higher harmonics are observed in l. Thin highly stratified layers, which carry most shear, last longer than near-homogeneous patches. In the reduced range [f, $N_{min} = 2f_h$], $\approx [\sigma_{min}, \sigma_{max}]$ including effects of non-traditional terms in weakly stratified waters (LeBlond and Mysak, 1978), a + 2/3-slope is dominant for the spectral continuum in this layer. The lower-layer spectral slope of + 2/3 continues to $2N_{min} \approx 4f_h$ if one ignores the $2f_h/M_2 + f^*$ sub-peak. This is reasonable because it is the background spectral slope from which peaks may be ignored (peaks follow a steeper slope). Both $2f_h$ and $4f_h$ are limits of minimum stratification following linear and non-linear stability conditions.

The harmonic peaks fall-off at a steeper slope of − 1/3, i.e. − 2 in an unscaled log-log plot, or steeper, although disruptions in the sequence are noticed. Even when the harmonic peaks are ignored, the IWB [f, N] (N >> f) demonstrates larger variance variability than the instrumental 95 % significance range, which implies alternating coherent and non-coherent portions in both layers throughout the instrumented range.

The associated coherence over 100-m vertical scales (Fig. 9b) shows moderate values of about 0.4–0.6 that exceed the significance level of 0.15, except for the semidiurnal peak which only becomes moderately coherent for vertical scales of 250 m and larger. A bulge

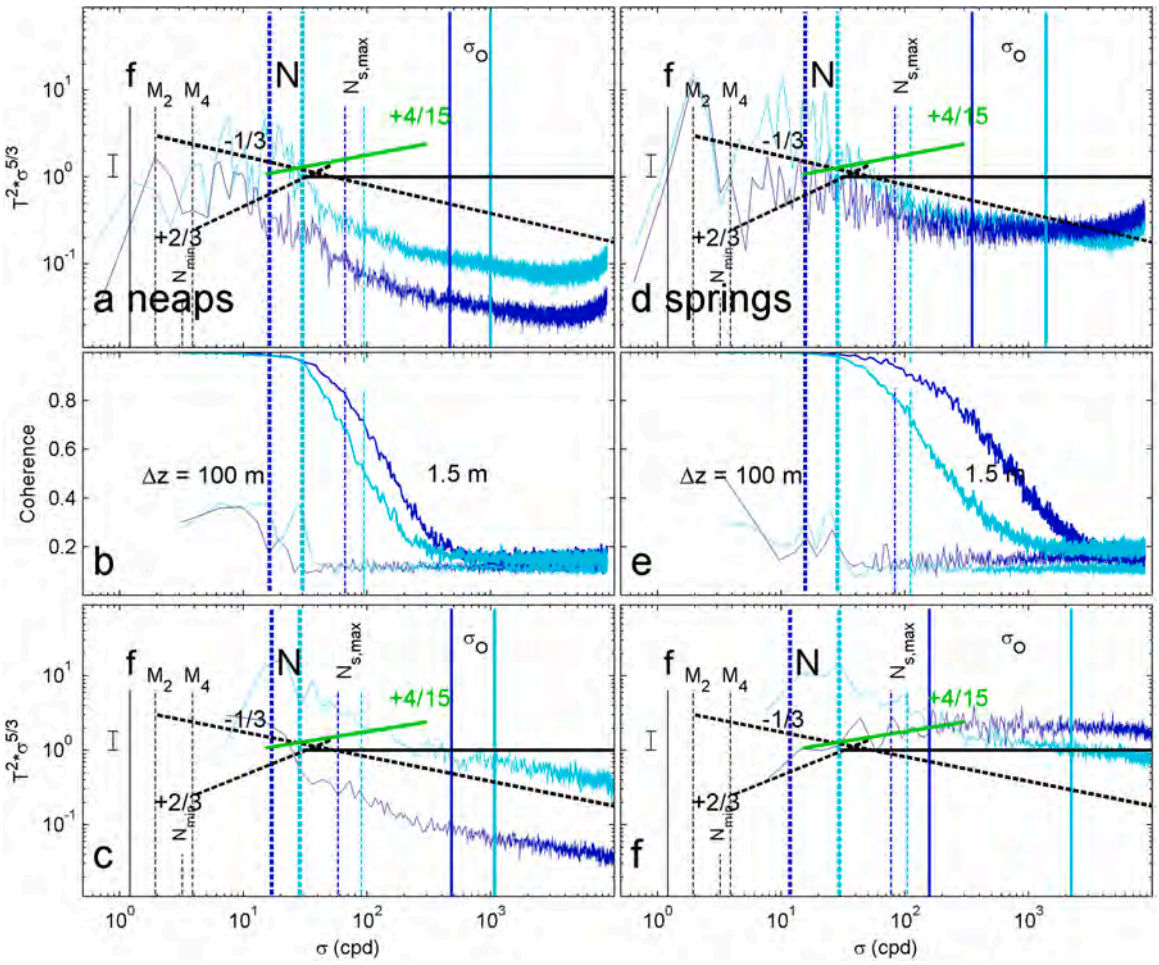

Fig. 10. As Fig. 9, but for detailed sub-sets of data. Left column shows data during neap tide, right column data during spring tide. (a) Log-log plot of T-variance from 0.2-Hz subsampled data as in Fig. 5 scaled with the inertial subrange slope − 5/3 (horizontal black line) and considerably smoothed (350 dof). $N_{s,max}$ denotes maximum 1.5-m-scale buoyancy frequency, σ_O is the Ozmidov frequency. (b) Associated coherence for data from a. between all possible pairs of Δz = 1.5-m (thick-line graphs) and 100-m (thin-line graphs) separated T-sensors. (c) As a., but for 3.6-h, 1-Hz sampled subset in Fig. 7a,b. (d) As a., but for data from Fig. 6. All slopes are identical as in a., for reference, but vertical lines show locally calculated values (except for M_2, M_4). (e) As b., but for data from d. (f) As c., but for data from Fig. 7c,d. Note relatively low N for l.

of somewhat increased coherence is seen in the range [N_{min}, N], best visible in data from u. The alternating coherent and non-coherent portions in the IWB are also visible, with coherent values at inertial-tidal higher harmonics as well as at some less well-distinguished frequencies. Only in u, a bulge is observed between about [12 cpd, N], evidencing 100-m coherent high-frequency internal waves as were observed in t,z-plots of w. In l, but barely in u, significant coherence is found at f.

The associated phase difference (Fig. 9c) is distributed over all values [− 180°, 180°] for $\sigma < \sigma_{min}$ and for $\sigma > N$, which confirms that coherence at 100-m vertical scales is insignificant at these frequencies. (The narrower the phase distribution over a frequency range, the larger the coherence). In the range [σ_{min}, σ_{max}], the mean phase difference is close to zero in both layers around particular frequencies, with almost exactly zero phase difference in the semidiurnal band [1.85, 2.05] cpd. In the range [N_{min}, N] in u mainly, a relatively narrow phase difference is observed at frequencies of the N-bulge. In the range [N_{min}, 12 cpd] mean phase difference increases above zero and shows a wider distribution between − 30° and 50°, slightly wider in l. This apparently associates with the moderate coherence at quasi-erratically distributed frequencies.

Resuming, Fig. 9 demonstrates that: The background internal wave spectral continuum for T-variance from u in the ocean-interior scales like σ^{-1}, not σ^{-2}, and that (harmonic) peaks average to a σ^{-2} scaling. Near the sloping seafloor, the IWB spectral background is dominated by shear-induced turbulence that is moderately coherent at 100-m vertical scales and also at erratic, non-harmonic frequencies. More details are investigated for particular periods thereby further focusing on the transition to turbulence using less subsampled data sets.

3.4.2. *Short-period mean spectra*

During neap tide, T-variance drops steeply at local N (Fig. 10a). Although mean variance is larger by about half an order of magnitude between u and l at all except at semidiurnal ($\sigma < N_{min} = 2f_h$) frequencies, the two spectra are quite similar in shape and spectral slopes. Within the IWB, between $N_{min} < \sigma < N$, the spectra (from u) roughly slope like + 2/3, or − 1 in an unscaled log-log plot. At super-buoyancy frequencies $\sigma > N$, the initially steep negative slope << − 1/3 slowly changes to − 1/3 at local maximum small-scale buoyancy frequency $N_{s,max}$. This slope, which is equivalent to − 2 in an unscaled log-log plot, cannot represent freely propagating internal waves here and must associate with fine-structure contamination (Phillips, 1971) of alternating stratified layers being advected past the T-sensors. Around 1000 cpd, the spectra become horizontal and attain a small inertial subrange before the upward turn to white noise that is affected by σ_{Nyq}. Inside the IWB [f, N], the variance variation between the frequencies exceeds the spectral significance level of noise variation by a factor of about two. The spectrum is not smooth, but shows peaks at undetermined frequencies, except for broadband N.

Between 500 and 600 cpd, the 1.5-m-scale coherence drops to insignificant levels (Fig. 10b). Over this vertical separation distance, significant coherence is larger in l than in u. This is reversed over a vertical separation distance of $\Delta z = 100$ m. The reversal occurs over about $\Delta z = 10$-m separation (20 m during spring tide). Over $\Delta z = 100$ m, coherence is barely significant except in the IWB, and it is insignificantly different from noise at $\sigma > 1.3N$.

A 3.6-h detail spectrum shows a larger discrepancy of one order of magnitude between u and l, but with the same spectral slopes that do not show a turbulence inertial subrange for the 150-m vertically averaged spectra (Fig. 10c).

During spring tide (Fig. 10d), T-variance shows higher levels in both layers at virtually all frequencies compared to neap tide, except at N_{min}. With the larger semidiurnal variance a + 2/3 slope is not well visible in the IWB. The variance variation within this band is more than a factor of two larger than the statistical significance level of noise variation, and remains higher by about a factor of 1.3 at $\sigma > N$, compared to neap tide. While the spectrum from u basically shows the same shape and slopes during spring tide as during neap tide, the spectrum from l is quite different during spring tide. In comparison with u, l shows less variance in the IWB, except at M_4, and up to $\sigma < N_{s,max} = 100$ cpd. At $\sigma > N_{s,max}$, it shows more variance, if it was scaled with N. For $\sigma > 1000$ cpd, it shows more variance, also in absolute (unscaled) spectra.

The T-variance from l does not show a bulge or wide peak between [N_{min}, N] including a steep drop for $\sigma > N$. Instead, slopes are observed of − 1/3, for $N < \sigma < N_{s,max}$, and 0, for $N_{s,max} < \sigma < 3000$ cpd. The extended inertial subrange of zero slope reflects the strong turbulent mixing by internal wave breaking at the seamount, as waves become more non-linear during spring tide. A transfer of (u) internal wave variance to (l) turbulence is suggested. However, the − 1/3 slope is surprising where one would expect a convective subrange with slope + 4/15 (− 7/5 in an unscaled log-log plot). Apparently, the mean of mixing is not large enough, as convection is only found in short periods of vigorous internal wave breaking (see below).

During spring tide, the mean coherence is similar to during neap tide, except that the coherence over $\Delta z = 1.5$-m separation distance extends to higher frequencies by nearly one order of magnitude (Fig. 10e). The transition frequency range, in which high-coherence > 0.95 becomes insignificant at coherence < 0.2, spreads over more than one order of magnitude and is observed entirely within the inertial subrange (for l). The distinction between u and l is more pronounced, with some weakly significant peaking around N, $N_{s,max}$ in coherence over 100-m separation distance in l.

In Fig. 10f, the spectra from 3.6-h data during spring tide show the inertial subrange until roll-off at about 10,000 cpd (instead of going up at σ_{Nyq}). Between [1000, 10,000] cpd, T-variance variation is less than the statistical significance spread, while being larger in the range [N, 100 cpd]. The high T-variance due to internal wave breaking in l shows a suggestion of + 4/15 slope in the range [40,400] cpd. It also shows an inertial subrange for $\sigma > 400$ cpd. The latter is partially also found in u and suggests some coupling between l and u in which shear-induced turbulence is driven simultaneously.

The transition in l from convective to shear-induced turbulence occurs at the Ozmidov frequency $\sigma_O = U/L_O$, which is computed using the local mean current-flow speed observed by ADCP. The σ_O separates anisotropic quasi-2D stratified turbulence from isotropic 3D turbulence in the inertial subrange. During the short period of spring-tide data for Fig. 10f, $L_O = 16$ m. In u during spring tide and in both layers during neap tide, T-spectra scale like σ^{-2} for $\sigma < \sigma_O$. For these layers and periods, $L_O = 1$–2 m and is less well resolved. This

σ^{-2}-scaling may be attributed to internal wave dominating over anisotropic turbulence for $\sigma < N_{s,max,}$ and to fine-structure contamination dominance for $N_{s,max} < \sigma < \sigma_O$. Only during spring tide a clear inertial subrange is observed for $\sigma > \sigma_O$ in l in (Fig. 10d). Data from u during spring tide and both layers during neap tide barely show an inertial subrange, despite the evident sporadic overturning in the t,z-images.

3.4.3. Cross-correlating

The overall cross-correlation of a 1.6-day segment during spring tide is dominated by tidal motions and demonstrates a substantial coupling (Fig. 11). However, the cross-correlation results separate the 1140-m vertical range in two sections: One extending from the seafloor up to about 1900 m, the other extending upward from 1750 m. Both show significant correlation over a range of up to ± 450 m. In the interlayer, the cross-correlation is limited in the vertical to a range of ± 150 m. This interlayer reaches from below just into the layer [1600,1800] m in which internal KHi-inducing hydraulic jumps with turbulent cores between [1650 1750] m are observed in Fig. 6.

4. Discussion

While internal wave breaking is the main source of turbulence in the vicinity of a large seamount, as evaluated from the turbulent overturning and the extent above the sloping seafloor, its effects horizontally or vertically are under research. Following reasoning in Armi (1979) and Garrett (1990) a 100-m thick boundary above sloping topography with 30-times larger turbulence intensity than in the ocean-interior would be sufficient to maintain the ocean stratification. Such intensities are easily reached here. Similarly, 1100-m average values are easily 3 times larger than ocean-interior values. Internal wave breaking and associated turbulent mixing including rapid restratification above sloping topography seems efficient enough to provide sufficiently high turbulence levels for the entire ocean.

Along isopycnals, layers of alternating weaker and stronger stratification do not last long, also because they are moved up and down by multiple internal waves, which also cause shear and thereby turbulent exchange. The layers do not last as long as suggested in the cartoon of Armi (1979) for flow around a seamount, as suggested by Schmitt et al. (1986) around a warm-core ring, and in the Caribbean (Schmitt, 1987) where they were estimated to be traceable over distances of 200 km. Such long-lasting layers cannot exist in the present data given the intense turbulent mixing. The mixing does not last longer than (local) minimum buoyancy period T_{Nmin} for active turbulence, after which restratification occurs. It results in a cartoon with small scales and thin layers like in Fig. 12a. This also follows from merging and diverging of thin-layer stratification over these short periods, and associated small distances. It corresponds with the layers observed by Dale et al. (2006) that stretched only about 1.5 km horizontally, lasting less than an inertial period. The 1.5-km horizontal scale is the value of the Rossby radius of deformation for a vertical mixing scale of 100 m, and the value of the

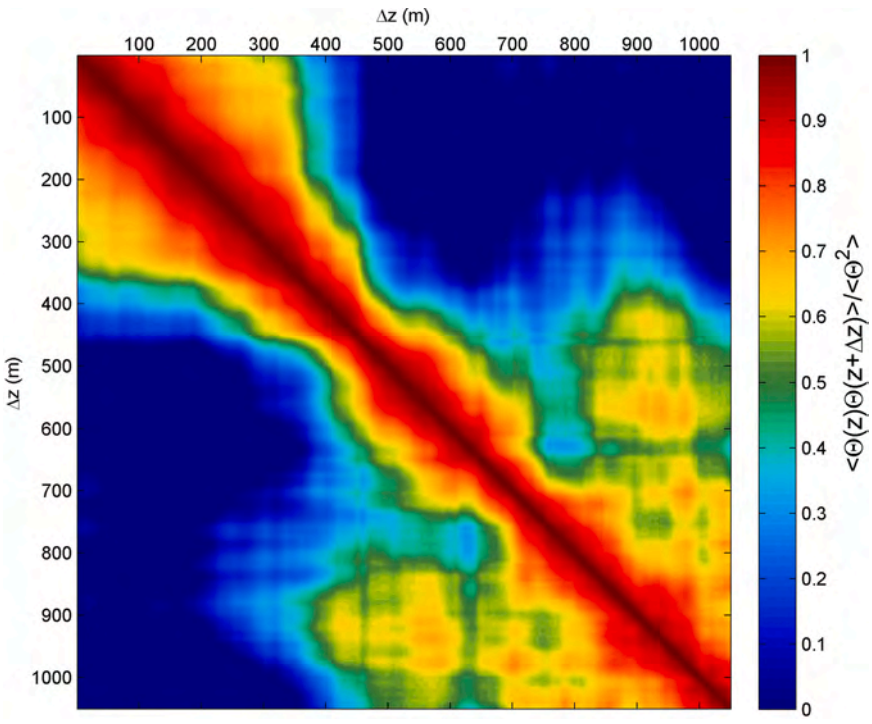

Fig. 11. Cross-correlation pattern of Conservative Temperature for separation distances Δz across the entire vertical range of T-sensor observations using data from the 1.6-d spring-tide period in Fig. 6.

buoyancy-scale-influenced horizontal extent of internal wave breaking (Winters, 2015).

In the vertical, the combined non-linear waves with main semidiurnal component extend several 100 m from the seafloor. During spring tide, increased turbulence intensity reaches up to 500 m above the seafloor, so that the Rossby radius of deformation becomes 8 km. Thereby, associated shear affects the internal waves above into local internal hydraulic jumps well away from topography, and thus well away from topography-generated flow-obstruction. The shear also causes short-duration isopycnal transport disruption. Close to the seafloor, reduction in turbulence is not observed down to 8 m from it in tidally averaged profiles. In the layer 8–30 m above the seafloor, near-homogeneous and well-stratified layers rapidly alternate, never lasting longer than 2.5 h. These near-slope observations evidence the dominance of internal wave breaking over frictional flows in turbulence generation and potential sediment resuspension at a sloping seafloor.

Following the observations of highly intermittent patchiness in internal tidal beams.

extending at least 20–30 km away from steep topography (van Haren et al., 2010), the present observations suggest the cartoon in Fig. 12b. Internal wave breaking and internal wave generation occur at similar slopes. Propagating internal waves emanate from above and below. In the interior, wave focusing due to vertically changing propagation directions may lead to local strongly non-linear interaction causing increased turbulence sporadically. In general, small-scale mixing is apparent everywhere in the interior, while in interplay with omnipresent internal wave (shear and straining). The abundant non-linearity on the one hand leads to coupled higher tidal/inertial harmonics. The flow around the seamount contributes quasi-permanent positive relative vorticity leading to blue-shifted near-inertial motions. On the other hand, the σ^{-1} spectral slope of the background internal wave continuum may correspond with the mathematical model of self-organized criticality (Bak et al., 1987). It is noted that Fig. 12 should not be misinterpreted for its one-sided simplicity as internal wave breaking occurs on all sides of a seamount.

5. Conclusions

The observations showed 1.6-d and 1140-m mean values of turbulence dissipation rate of 7–24 $\times$ 10^{-9} m^2 s^{-3}, from neap to spring tide. Between 8 and 108 m above the seafloor the 100-m mean value-range was 14–74 $\times$ 10^{-9} m^2 s^{-3}. Similarly for eddy diffusivity, 4–15 $\times$ 10^{-4} m^2 s^{-1} for 1140-m means and 20–90 $\times$ 10^{-4} m^2 s^{-1} for lower 100-m mean values. The effects of the turbulence induced by internal wave breaking above the sloping seamount sides reach further than previously thought. Mean turbulence values decrease by half an order of magnitude over a vertical extent of about 500–600 m from the seafloor, and remain steady up to 1146 m above the seafloor at values more than one order of magnitude larger than found in the ocean-interior. The buoyancy frequency steadily decreases with depth, and is reduced by a factor of 2 between 1146 and 8 m above the seafloor. Vertical variability of N is observed over half an order of magnitude in layers of 100–200 m thick. Horizontally, elevated turbulence values reach at least 7 km horizontally from the seamount, nearly one order of magnitude further than intense turbulence modeled over supercritical slopes.

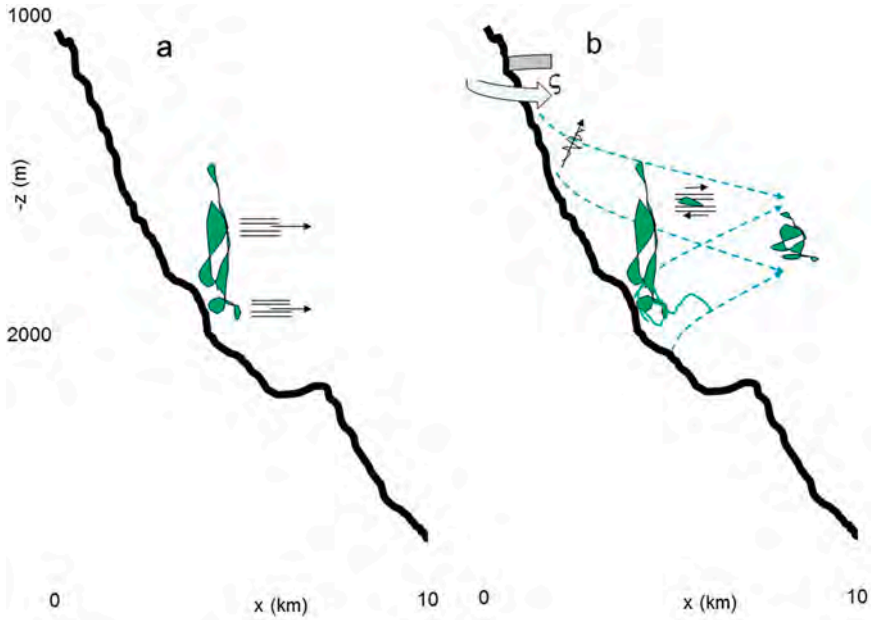

Fig. 12. Cartoon of internal wave breaking processes above a super-critical deep-sea slope. (a) Intensive turbulence generation up to 500 m above the seafloor extending horizontally about 1.5 km, following Winters (2015). Turbulence may be transported to the interior along isopycnals in thin layers. Turbulent overturning is schematized in green patches as in Fig. 1. (b) The present data demonstrate the vigorous turbulence at the seafloor of a. whereby also small-scale internal waves are generated. The interior shows continuous local turbulence generation, in part by small-scale shear and in part by internal waves generated at the slope of which energy is transported along characteristics and which interact strongly whereby higher harmonics are generated, most intensely during spring tide. The flow around the seamount contributes relative vorticity ς.

Largest isotherm excursions are found near the seafloor, with > 100 m amplitudes during spring tide. Isotherms are non-linear, reflecting the strong presence of higher tidal harmonics in temperature and current spectra, which are statistically significant to about M_{10}. Apparent but weaker inertial/tidal harmonics also indicate interactions between tidal and near-inertial motions. For the latter, the seamount seems to affect the local absolute vorticity of 1.083f. Away from the seafloor IWB T-variance scales like N^3, while near the seafloor the amplitude-enhanced semidiurnal tide scales like N.

In the upper layer, higher harmonics extent above an IWB continuum that scales like unsaturated open-ocean internal waves up to the buoyancy frequency, at which more than 100-m vertically coherent high-frequency internal waves are observed. In the lower layer, the IWB-continuum scales like open-ocean internal waves over a limited frequency range of only half an order of magnitude from the inertial frequency. It reflects the limited IWB in minimum stratification conditions. The remainder of the IWB-continuum scales like the turbulence inertial subrange, which suggests a dominant filling of the continuum with turbulent eddies, and which explains the erratically alternating coherent and non-coherent portions in that frequency range.

Although small-scale mixing is observed in the interior that may be associated with isopycnal transport, turbulence dominance over waves is mainly found during spring tide. The turbulence is mainly shear-induced, with convection being dominant during brief periods of strong overturning only. When convection occurs, (shear-induced) turbulence also dominates over fine-structure contamination in the upper layer, which suggests a coupling between lower and upper layers over a vertical distance of at least 500 m. During spring tide, vertical phase differences in cross-slope current component and temperature change sign around 1800 m. Thus, a focusing of internal tidal energy is expected that associates with strongly non-linear hydraulic jumps following flow-obstruction well away from topography leading to intensified mixing in the interior. As a result, propagating internal waves emanating from the steep topography drive, after breaking, interior mixing that exceeds the turbulence intensity of mixed waters transported along isopycnals.

Along isopycnals, layers are not longer-lived than one inertial period, before becoming merged or strained by internal waves. Sporadic internal wave mixing other than via focused internal tides cause continued small-scale mixing of the layers.

Declaration of Competing Interest

The authors declare that they have no known competing financial interests or personal relationships that could have appeared to influence the work reported in this paper.

Data Availability

Data will be made available on request.

Acknowledgements

I thank the captain and crew of the R/V Pelagia and NIOZ-NMF for their very helpful assistance during deployment and recovery. This research was supported in part by NWO, the Netherlands Organization for Scientific Research.

References

Alford, M.H., Pinkel, R., 2000. Overturning in the thermocline: the context of ocean mixing. J. Phys. Oceanogr. 30, 805–832.
Armi, L., 1978. Some evidence for boundary mixing in the deep ocean. J. Geophys. Res. 83, 1971–1979.
Armi, L., 1979. Effects of variations in eddy diffusivity on property distributions in the oceans. J. Mar. Res. 37, 515–530.
Aucan, J., Merrifield, M.A., Luther, D.S., Flament, P., 2006. Tidal mixing events on the deep flans of Kaena Ridge, Hawaii. J. Phys. Oceanogr. 36, 1202–1219.
Bak, P., Tang, C., Wiesenfeld, K., 1987. Self-organized criticality: an explanation of the 1/f noise. Phys. Rev. Lett. 59, 381–384.
Bolgiano, R., 1959. Turbulent spectra in a stably stratified atmosphere. J. Geophys. Res. 64, 2226–2229.
Cael, B.B., Mashayek, A., 2021. Log-skew-normality of ocean turbulence. Phys. Rev. Lett. 126, 224502.
Chalamalla, V.K., Sarkar, S., 2015. Mixing, dissipation rate, and their overturn-based estimates in a near-bottom turbulent flow driven by internal tides. J. Phys. Oceanogr. 45, 1969–1983.
Cimatoribus, A.A., van Haren, H., 2015. Temperature statistics above a deep-ocean sloping boundary. J. Fluid Mech. 775, 415–435.
Dale, A.C., Levine, M.D., Barth, J.A., Austin, J.A., 2006. A dye tracer reveals cross-shelf dispersion and interleaving on the Oregon shelf. Geophys. Res. Lett. 33, L03604 https://doi.org/10.1029/2005GL024959.
Dillon, T.M., 1982. Vertical overturns: a comparison of Thorpe and Ozmidov length scales. J. Geophys. Res 87, 9601–9613.
Eden, C., Pollmann, F., Olbers, D., 2019. Numerical evaluation of energy transfers in internal gravity wave spectra of the ocean. J. Phys. Oceanogr. 49, 737–749.
Eriksen, C.C., 1982. Observations of internal wave reflection off sloping bottoms. J. Geophys. Res. 87, 525–538.
Galbraith, P.S., Kelley, D.E., 1996. Identifying overturns in CTD profiles. J. Atmos. Ocean. Technol. 13, 688–702.
Garrett, C., 1990. The role of secondary circulation in boundary mixing. J. Geophys. Res. 95, 989–993.
Garrett, C., Munk, W., 1972. Space-time scales of internal waves. Geophys. Fluid Dyn. 3, 225–264.
Gregg, M.C., D'Asaro, E.A., Riley, J.J., Kunze, E., 2018. Mixing efficiency in the ocean. Ann. Rev. Mar. Sci. 10, 443–473.
van Haren, H., 2007. Monthly periodicity in acoustic reflections and vertical motions in the deep ocean. Geophys. Res. Lett. 34, L12603 https://doi.org/10.1029/2007GL029947.
van Haren, H., 2017. Exploring the vertical extent of breaking internal wave turbulence above deep-sea topography. Dyn. Atmos. Oceans 77, 89–99.
van Haren, H., 2018. Philosophy and application of high-resolution temperature sensors for stratified waters. Sensors 18, 3184. https://doi.org/10.3390/s18103184.
van Haren, H., Gostiaux, L., 2009. High-resolution open-ocean temperature spectra. J. Geophys. Res. 114, C05005 https://doi.org/10.1029/2008JC004967.
van Haren, H., Gostiaux, L., 2012. Detailed internal wave mixing observed above a deep-ocean slope. J. Mar. Res. 70, 173–197.
van Haren, H., Maas, L.R.M., Gerkema, T., 2010. Patchiness in internal tidal beams. J. Mar. Res. 68, 237–257.
IOC, SCOR, IAPSO, 2010. The International Thermodynamic Equation of Seawater – 2010: Calculation and Use of Thermodynamic Properties. Intergovernmental Oceanographic Commission, Manuals and Guides No. 56, UNESCO, Paris, France, 196 pp.

Klymak, J.M., Pinkel, R., Rainville, L., 2008. Direct breaking of the internal tide near topography: Kaena Ridge, Hawaii. J. Phys. Oceanogr. 380–399.
Kolmogorov, A., 1941. The local structure of turbulence in incompressible viscous fluid for very large Reynolds' numbers. Dokl. Akad. Nauk SSSR 30, 301–305.
Krauss, W., 1966. Interne Wellen, Borntraeger, Berlin-Nikolassee, pp. 248.
LeBlond, P.H., Mysak, L.A., 1978. Waves in the Ocean. Elsevier, New York, p. 602.
Levine, M., Boyd, T.J., 2006. Tidally forced internal waves and overturns observed on slope: results from HOME. J. Phys. Oceanogr. 36, 1184–1201.
Li, S., Li, H., 2006. Parallel AMR Code for Compressible MHD and HD Equations. T-7, MS B284, Theoretical division, Los Alamos National Laboratory. ⟨http://citeseerx.ist.psu.edu/viewdoc/summary;jsessionid=1548A302FD5C2B1DFAC1BA7A5E70605F?doi=10.1.1.694.3243⟩, (Accessed 17 May 2022).
MacCready, P., Rhines, P.B., 1991. Buoyant inhibition of Ekman transport on a slope and its effect on stratified spin-up. J. Fluid Mech. 223, 631–651.
Mater, B.D., Venayagamoorthy St, S.K., Laurent, L., Moum, J.N., 2015. Biases in Thorpe scale estimation of turbulence dissipation. Part I: assessments from large-scale overturns in oceanographic data. J. Phys. Oceanogr. 45, 2497–2521.
Matsumoto, Y., Hoshino, M., 2004. Onset of turbulence by a Kelvin-Helmholtz vortex. Geophys. Res. Lett. 31, L02807 https://doi.org/10.1029/2003GL018195.
McComas, C.H., Bretherton, F.P., 1977. Resonant interaction of oceanic internal waves. J. Geophys. Res. 82, 1397–1412.
Munk, W., 1966. Abyssal recipes. Deep-Sea Res. 13, 707–730.
Munk, W., 1981. Internal waves and small-scale processes. In: Warren, B.A., Wunsch, C. (Eds.), Evolution of Physical Oceanography. MIT Press, Cambridge, MA, pp. 264–291.
Nash, J.D., Alford, M.H., Kunze, E., Martini, K., Kelly, S., 2007. Hotspots of deep ocean mixing on the Oregon. Geophys. Res. Lett. 34, L01605 https://doi.org/10.1029/2006GL028170.
Oakey, N.S., 1982. Determination of the rate of dissipation of turbulent energy from simultaneous temperature and velocity shear microstructure measurements. J. Phys. Oceanogr. 12, 256–271.
Osborn, T.R., 1980. Estimates of the local rate of vertical diffusion from dissipation measurements. J. Phys. Oceanogr. 10, 83–89.
Ozmidov, R.V., 1965. Some peculiarities of the energy spectrum of oceanic turbulence. Dokl. Akad. Nauk SSSR 161, 828–831.
Pawar, S.S., Arakeri, J.H., 2016. Kinetic energy and scalar spectra in high Rayleigh number axially homogeneous buoyancy driven turbulence. Phys. Fluids 28, 065103.
Perfect, B., Kumar, N., Riley, J.J., 2018. Vortex structures in the wake of an idealized seamount in rotating, stratified flow. Geophys. Res. Lett. 45, 9098–9105. https://doi.org/10.1029/2018GL078703.
Phillips, O.M., 1971. On spectra measured in an undulating layered medium. J. Phys. Oceanogr. 1, 1–6.
Phillips, O.M., 1977. The Dynamics of the Upper Ocean, 2nd ed. Cambridge University Press, Cambridge, UK, p. 336.
Platzman, G.W., 1964. An exact integral of complete spectral equations for unsteady one-dimensional flow. Tellus 16, 422–431.
Sarkar, S., Scotti, A., 2017. From topographic internal gravity waves to turbulence. Ann. Rev. Fluid Mech. 49, 195–220.
Schmitt, R.W., 1987. The Caribbean sheets and layers transects (C-SALT) Program. EOS 68, 57–60.
Schmitt, R.W., Lueck, R.G., Joyce, T.M., 1986. Fine- and microstructure at the edge of a warm-core ring. Deep-Sea Res. 33, 1665–1689.
Schuster, H.G., 1984. Deterministic Chaos: An Introduction. Physik Verlag, Weinheim, p. 220.
Smith, W.H.F., Sandwell, D.T., 1997. Global seafloor topography from satellite altimetry and ship depth soundings. Science 277, 1957–1962.
Tennekes, H., Lumley, J.L., 1972. A First Course in Turbulence. The MIT Press, Boston, p. 293.
Thorpe, S.A., 1977. Turbulence and mixing in a Scottish loch. Philos. Trans. Roy. Soc. Lond. A 286, 125–181.
Thorpe, S.A., 1987. Transitional phenomena and the development of turbulence in stratified fluids: a review. J. Geophys. Re.s 92, 5231–5248.
Warhaft, Z., 2000. Passive scalars in turbulent flows. Annu. Rev. Fluid Mech. 32, 203–240.
Weatherly, G.L., Martin, P.J., 1978. On the structure and dynamics of the oceanic bottom boundary layer. J. Phys. Oceanogr. 8, 557–570.
Winters, K.B., 2015. Tidally driven mixing and dissipation in the boundary layer above steep submarine topography. Geophys. Res. Lett. 42, 7123–7130. https://doi.org/10.1002/2015GL064676.
Wunsch, C., 1970. On oceanic boundary mixing. Deep-Sea Res. 17, 293–301.
Wunsch, C., 1972. Temperature microstructure on the Bermuda slope with application to the mean flow. Tellus 24, 350–367.
Wunsch, C., Dahlen, J., 1970. Preliminary results of internal wave measurements in the main thermocline at Bermuda. J. Geophys. Res. 75, 5899–5908.